Exploring the sensitivity of the vanadium redox proxy to Fe/Mn-(oxyhydr)oxide cycling in a basinal oxic margin setting

Nicol. D. Udy[1*], Sune G. Nielsen[2,3], Maureen Auro[2], Kasper P. Olesen[1], Donald E. Canfield[1]

[1] Department of Biology, Nordcee, University of Southern Denmark, Odense, Denmark

[2] Department of Geology and Geophysics, Woods Hole Oceanographic Institution, Woods Hole, MA, USA

[3]Centre de Recherches Pétrographiques et Géochimiques, CNRS, Université de Lorraine, Nancy, France

* nicoldudy_phd_correspondence@proton.me (corresponding author)

This is a non peer-reviewed pre-print, presently under review for publication in *Geochimica et Cosmochimica Acta.*

Abstract

Accurately interpreting the redox state of ancient seawater using the Vanadium (V) paleo-redox proxy requires us to have a comprehensive understanding of the sinks that might impact vanadium's cycling in the ancient ocean. Ferromanganese (oxyhydr)oxides accumulating in sediments beneath oxic seawater probably constitute the largest modern sink of marine V. In many oxic sediment sinks, V enrichments are low relative to the crustal background, and authigenic $\delta^{51}V$ values (where $\delta^{51}V$ = 1000 ‰ * [($^{51}V/^{50}V_{Sample} - {}^{51}V/^{50}V_{Alfa\text{-}aesar}$)/($^{51}V/^{50}V_{Alfa\text{-}aesar}$)]) are offset from seawater $\delta^{51}V$ by -1.1 ‰. However, recent evidence supports the existence of an efficient V-Fe-Mn-(oxyhdyr)oxide sink on some portions of the oxic continental margin (OCM). Prior to the observation of V enrichments in the aforementioned OCM sediments, efficient V removal from oxic seawater had primarily been described near hydrothermal plumes and seeps. Moreover, most of the OCM is likely not enriched in V, implying that OCM V enrichment may be produced by an unconstrained, and potentially inhomogeneous, V sink. One such V enriched OCM basin can be found in the Skagerrak seaway, located between Norway and Denmark. In this study, we report $\delta^{51}V$ values and V, Mn, and Fe concentrations from sediments collected from the shelf, slope, and deep basin of the Skagerrak. Elemental concentrations were measured from porewaters, and from sediment solids using a novel sequential extraction method that distinguishes between V bound to Fe- and Mn- (oxyhydr)oxides.

Vanadium sequestration rates into the deep basin of the Skagerrak are at least 10x higher than rates reported from typical OCM sediments. Authigenic V delivery into the Skagerrak basin is primarily driven by an allochthonous Fe-(oxyhydr)oxide sink that reproduces the typical V-(oxyhydr)oxide isotopic fractionation factor of -1.1 ‰. Additionally, we hypothesize that Mn-oxides precipitating from Mn^{2+} effluxing from shelf sediments enhance the V sink in the deep basin of the Skagerrak. Authigenic V concentrations are dominated by Mn-oxides in the top sediment of the Skagerrak basin, the only sediments in our data set where Mn concentrations are diagenetically enriched enough to approach Fe concentrations. These deep basin top sediments display a unique authigenic V isotope fractionation relative to seawater <0.9‰, suggesting that V-Mn-oxide precipitation may attenuate the V isotopic fractionations typically induced by adsorption onto (oxyhydr)oxide minerals. The allochthonous Fe-(oxyhydr)oxide V sink increases in importance from shelf → basin while the diagenetic Mn-oxide V sink is uniquely important in the basin, suggesting that a basin shaped hydrography may be one critical factor enhancing V delivery into OCM sediments. Much of the sedimentary archive heretofore analyzed for V was deposited in epicontinental basins. Caution should therefore be applied when using V to interpret the redox state of the ancient seawater that

once over lied sediments depositing in basins. Moreover, our results imply that Mn-oxides will be an important V sink from seawater when they are diagenetically enriched, and that diagenetically precipitated (oxyhydr)oxides in general may induce distinct, and previously unrecognized, V isotopic fractionations from seawater.

keywords: Vanadium cycling; Vanadium isotopes; paleo-redox proxy; diagenesis; continental margin

1 Introduction

Reliable geochemical proxies for marine redox conditions can constrain the chemical and biological processes that operated in ancient oceans, supporting efforts to resolve the history of Earth's oceanic and atmospheric chemistry. The concentration and isotopic composition of the redox-sensitive metal vanadium (V), as preserved in the paleo-record, are currently being used as proxies for ancient seawater redox chemistry (e.g. Li et al., 2023; Wei et al., 2023; Heard et al., 2023; Fan et al., 2021; Han et al., 2018; Ostrander et al., 2017). Presently, models of global marine V cycling assume that sinks in anoxic seawater will remove V from the ocean efficiently compared to sinks in oxic seawater (Little et al., 2025; Nielsen, 2021). As a consequence, the isotopic composition and concentration of V dissolved in seawater is expected to be particularly sensitive to changes in ocean anoxia over geologic time (Nielsen, 2021).

The analysis summarized above is based on a paucity of V concentrations measured from modern marine sediments (i.e. V_{Sed}), spread amongst depositional environments with different redox chemistries (e.g. Little et al., 2025; Nielsen, 2021; Bennett and Canfield, 2020). Namely, sediments underlying anoxic seawater consistently show V_{Sed} enrichments (Nielsen, 2021; Bennett and Canfield, 2020) relative to the upper crustal background (e.g. Rudnick and Gao, 2014), while sediments underlying oxic seawater often show V_{Sed} enrichments consistent with or slightly above (Nielsen, 2021; Bennett and Canfield, 2020) the crustal background. Important exceptions to the dependency of V_{Sed} enrichments on anoxia in overlying waters have been recognized. For example, dissolved V can become depleted in restricted anoxic water columns, limiting V_{Sed} enrichments in underlying sediments (Bennett and Canfield, 2020; Calvert and Pedersen, 1993). Furthermore, V_{Sed} can become enriched in sediments near hydrothermal plumes despite oxic seawater conditions (Trefry and Metz, 1989), as reviewed in more detail below. Applying the V redox proxy, therefore, requires careful consideration of how vanadium's geochemical signal is sensitive to water column

redox conditions, and when other factors may influence V geochemical signals in the sedimentary archive.

Recent data published from some portions of the oxic continental margin (OCM) highlight another potential exception to the dependency of V_{Sed} enrichments on anoxia in overlying waters. Some OCM sediments not impacted by hydrothermal activity, recently analyzed for V_{Sed}, yield V enrichments comparable to those reported from sediments impacted by both hydrothermal activity and anoxic seawater (Paul et al., 2024; Li et al., 2021; Bennett and Canfield, 2020). Considering these most recent data, the OCM should not be treated as a homogenous environment regarding V geochemistry. The potential mechanisms responsible for enriching V on the OCM, and their importance relative to one another, have yet to be established, and therefore cannot easily be incorporated into models of global V cycling. These processes must be identified in order to understand their relevance to V geochemical signals in sedimentary archives, and to better understand V cycling in the modern ocean.

Vanadium is primarily removed from seawater by particulate scavenging (Crans et al., 1998; Wanty and Goldhaber, 1992; Baes and Mesmer, 1976) that is less efficient in the presence of oxygen due to the redox chemistry of V (Wehrli and Stumm, 1989). Above concentrations of 10 µm dissolved O_2 (Wehrli and Stumm, 1989) vanadate dominates the dissolved V pool, typically speciating as the highly soluble oxyanion $H_2VO_4^-$ (Breit and Wanty, 1991; Shaw et al., 1990; Wehrli and Stumm, 1989). As evidence of its high solubility, vanadate shows a homogenous global concentration of ~1.8 µg L^{-1} in oxic seawater (Li et al., 2025; Ho et al., 2018; Middelburg et al., 1988; Collier, 1984) with a residence time of roughly 91 kyr, almost two orders of magnitude higher than the mixing time of the global ocean (Nielsen, 2021). Despite the solubility of vanadate, most V sequestered into sediments from the modern ocean is believed to be removed from oxic seawater, by an inefficient but globally ubiquitous ferromanganese (oxyhydr)oxide sink (Little et al., 2025; Nielsen, 2021).

The importance of Fe-(oxyhydr)oxides, in particular, for V removal from the ocean was first observed in hydrothermal plumes and sediments. Fresh, Fe-(oxyhydr)oxide rich particulates precipitating from various hydrothermal outflows host remarkably high V enrichments relative to crustal references (Feely et al., 1998; Trefry and Metz, 1989). Similarly high V enrichments are also present in sediments collected near these hydrothermal plumes (Trefry and Metz, 1989), directly connecting V enrichments in hydrothermally altered sediment sinks to V-Fe(oxyhydr)oxide

reactions in seawater. Comparably mild, but significant, V enrichments are also present in Fe- and Mn-rich pelagic clays (Chester and Jickells, 2012; Li and Schoonmaker, 2003; Thomson et al., 1984). It is these pelagic V enrichments, in combination with the extensive seafloor area covered by oxic pelagic waters, that have been used to estimate the large contribution of the oxic sink to annual rates of dissolved V removal from the modern ocean (Little et al., 2025; Nielsen, 2021).

However, the global importance of Fe-(oxyhydr)oxides relative to other potential particulate sinks, and the reactivity of (oxyhydr)oxides in all modern oxic environments, has not yet been resolved (Little et al., 2025; Nielsen, 2021). In many OCM and pelagic settings, the (oxyhydr)oxide minerals present in the water columns must constitute relatively unreactive phases, to explain the muted V enrichments observed from suspended particulates (Ho et al., 2018; Collier, 1984) and sediments (Bennett and Calfield, 2020; Thomson et al., 1984). In contrast, both Fe-(oxyhydr)oxides and Mn-oxides appear to be efficient V sinks from seawater along the Siberian Chukchi margin of the Arctic (Li et al., 2021). Specifically, V is enriched with Fe-(oxyhydr)oxides on suspended particulates (Whitmore et al., 2019) and in sediments (Li et al., 2021) on the shelf and is enriched with both Fe- and Mn- (oxyhydr)oxides in the deep basin (Li et al., 2021). Therefore, Mn-oxides might in fact compete with Fe-(oxyhydr)oxides as a V sink on some portions of the OCM, adding inhomogeneity to V cycling in oxic seawater.

In addition to water column processes, V sequestration onto Mn- and Fe- (oxyhydr)oxides has been described in relationship to diagenetic cycling within the sediment column (Morford et al., 2005; Morford and Emerson, 1999). Below the depth of oxygen penetration in sediments, dissimilatory Fe and Mn reduction results in the dissolution of (oxyhydr)oxide minerals and the release of reduced Fe(II) and Mn(II) into porewaters (e.g. Burdige, 1993; Lovley, 1991; Froelich et al., 1979). Any V adsorbed to these oxides will be liberated to porewaters as Fe/Mn dissimilation proceeds (Morford and Emerson, 1999), resulting in fluxes of dissolved Fe, Mn and V upwards in the sediment column (Morford et al., 2005). Up-fluxing Fe and Mn can re-precipitate as (oxyhydr)oxide minerals in the upper sediment column by reacting with oxygen, or in the case of Fe(II) with Mn-oxide (Burdige et al., 1993; Lovley, 1991). As dissolved V has been observed to co-precipitate with (oxyhydr)oxides in experimental settings (e.g. Shieh and Deudall, 1988; Takematsu et al., 1985), V enrichments in sediments could therefore also be related to oxide driven diagenesis. Thus, given the dual role of both Fe and Mn in sequestering V, and the chance that some sequestration could be related to early diagenesis, V-Fe-Mn couples in OCM sediments should be carefully evaluated before concluding they are related to sequestration of V from the water column.

Measuring vanadium's isotopic composition in V-enriched OCM sediments may further enhance our understanding of V cycling in oxic environments. Vanadium has two stable isotopes, ^{51}V (~99.75 %) and ^{50}V (~0.25 %). The isotopic composition of V is reported using delta notation ($\delta^{51}V$, ‰) (eq. 1):

$$\delta^{51}V = 1000\ ‰ * (^{51}V/^{50}V_{sample} - {}^{51}V/^{50}V_{AA})/ {}^{51}V/^{50}V_{AA} \quad \text{eq. 1.}$$

Here, the isotopic composition of a sample ($^{51}V/^{50}V_{sample}$) is related to the isotopic composition of the Alfa-Aesar (AA) standard solution ($^{51}V/^{50}V_{AA}$) (Nielsen et al., 2011; Prytulak et al., 2011). The $\delta^{51}V$ signature preserved in sediments should be sensitive to the specific processes driving the removal of V from seawater or from porewaters (Little et al., 2025; Wu et al., 2015). For example, authigenic V accumulating in oxic sediments is consistently depleted in ^{51}V ($\delta^{51}V_{Oxic}$ = -0.90 ± 0.1‰) (Wu et al., 2020) relative to seawater ($\delta^{51}V_{Oxic}$ = +0.20 ± 0.15‰) (Li et al., 2025; Wu et al., 2019). The observed difference is consistent with isotopic fractionation during adsorption of aqueous V to Fe-Mn-(oxyhydr)oxides (Wu et al., 2020). No diagenetic isotopic fractionations have yet been documented for V (Little et al., 2025). Therefore, OCM sediments enriched in V present a unique opportunity to test the sensitivity of $\delta^{51}V$ to enhanced sequestration in oxic seawater and/or to diagenetic recycling in sediments.

In this study, we report V_{Sed} concentrations and $\delta^{51}V$ from the sediments of the Skagerrak seaway, an OCM environment with a basin-shaped hydrography, known to host V, Mn and Fe enrichments (e.g. Canfield et al., 1993a,b; Rajendran et al., 1992). We present a novel sequential extraction method (Olesen et al., 2025) distinguishing between Al-bound, Mn-oxide bound, and Fe-(oxyhydr)oxide bound vanadium, allowing us to elucidate the roles of seawater sequestration and diagenesis in controlling vanadium's distribution within the sediments of the Skagerrak. In combination with porewater profiles and isotopic data, our analysis provides a wholistic view of V cycling in the Skagerrak, with important implications for V cycling along modern and ancient continental margins.

2 Site Description

The Skagerrak is a continental margin seaway, connecting the North Sea to the Kattegat and Danish straits (fig. 1). The southern portion of the Skagerrak is covered by a large expanse of shallow water (<100 m) subject to active erosion (Diesing et al., 2021). The sediment concentrations of fine particulates (Diesing et al., 2021; Hanebuth et al., 2015), organic matter (Diesing et al., 2021; Stahl

et al., 2004), and many metals – including V, Mn, and Fe (Siems et al., 2025; Sæther et al., 1996; Danielsson et al., 1999; Bengtsson and Stevens, 1996; Canfield et al., 1993b; Klaver et al., 1993; Magnusson et al., 1996) – increase with water depth into the regionally deep (>650 m) Norwegian Trench. The Norwegian Trench in the Skagerrak is separated from the North Sea by a 270 m deep sill (Longva and Thorsnes, 1997; Stevens et al., 1996), generating a basin in the northern portion of the seaway (fig. 1).

The basin of the Norwegian trench acts as the primary depocenter for particulate matter in the Skagerrak region (Diesing et al., 2021; Pederstad et al., 1993; Van Weering et al., 1987; Erlenkeuser and Pederstad, 1984). The composition of these sediments is controlled by at least three sources. First and primarily, currents circulating into the Skagerrak from the North Sea deposit their particulate loads beneath a central gyre forming over the Norwegian Trench (Eisma and Kalf, 1987; Fonselius, 1990; Gyllencreutz and Kissel, 2006; Longva and Thorsnes, 1997; Rodhe, 1987). Second, fine particulates sourced from shelf and upper-slope sediments may fall from suspension due to a reduction in bottom water current velocity in the trench (Hanebuth, 2015). There is evidence of sediment resuspension (Lepland and Stevens, 1996; Fengler et al., 1994; Paetzler, 1994; Canfield et al., 1993b) that may be transported into the basin of the Skagerrak by laminar currents flowing along the seafloor (Van Weering et al., 1993). Lastly, 15% or more of the sediment mass deposited in the Skagerrak can be ascribed to local river inflows and the Kattegat (Gyllencreutz and Kissel, 2006; Bengtsson and Stevens, 1996; Longva and Thorsnes, 1997; Lepland and Stevens, 1996; Pederstad et al., 1993).

The Skagerrak is an excellent test for how V geochemistry can be driven by differences in Fe- and Mn- (oxyhydr)oxide diagenesis. Moving from shelf to basin, solid sediment concentrations of Fe and Mn increase (e.g. Siems et al., 2025; Kristensen et al., 2018; Reyes et al., 2017; Dale et al., 2008; Knab et al., 2008; Thamdrup and Dalsgaard, 2000; Fengler et al., 1994; Canfield et al., 1993a,b), and Mn concentrations in basin sediments are high enough to exceed Fe concentrations (Canfield et al., 1993b). These high Mn concentrations are unusual, and the Mn is thought to derive from Mn^{2+} lost by diffusion from shelf sediments (Canfield et al., 1993b). Indeed, the basin of the Skagerrak is special in that dissimilatory Mn-reduction accounts for nearly all carbon oxidation in the deepest Mn-rich sediments (Canfield et al., 1993b), a situation only rarely observed in the modern ocean (Lovley, 1991). Moving southwards and into shallower water, dissimilatory Mn reduction is less important for carbon oxidation. Instead, slope and shelf sediments are dominated by iron and sulfate reduction (Canfield et al., 1993b). Sampling in the Skagerrak therefore allows us

to observe the behavior of vanadium in sediments experiencing variable Mn and Fe inputs, and variable rates of Mn-driven diagenesis and Fe-driven diagenesis, within the same depositional region.

3 Methodology

3.1 Sampling

We sampled a transect along the Skagerrak seaway aboard the *R/V Skagerrak*, between the 12th and 18th of December 2021. Three sites were sampled (fig. 1, tbl. 1), covering a range of biogeochemical, compositional, and hydrographic contexts present in the region. Site 4 (S4, 182 m water depth) was located on the Danish shelf. Sites 6 (S6, 392 m water depth) and 9 (S9, 687 m water depth) were located on the slope and in the basin of the Norwegian Trench, respectively. All three sites experience active sedimentation (Diesing et al., 2021).

All materials coming into contact with trace metal samples were acid washed in 1 M ultrapure HCl acid or were purchased with a trace-metal free certification and will hereafter be referred to as TM-clean. When sample filtration was necessary, disposable 0.2 μm cellulose acetate (CA) filters fitted with a 0.7 μm glass fiber pre-filter were used. Filters were pre-rinsed with 1 – 3 mL of the sample volume before collection. Filtered waters were then preserved through the addition of concentrated HNO_3 (2% HNO_3; 98% sample). Nitric acid used for sample preservation was purchased with a TM-clean certification and additionally distilled in house.

Seawater samples from each site were collected from a range of depths using a Sea-Bird Scientific carousel water sampler with mounted Niskin bottles. The bottles were not specially treated for trace-metal sampling, but the inner surface of the collection vessel was free of metal components. For each sampled depth, 10 mL water was removed from a Niskin bottle and filtered into 50 mL, TM-clean Falcon© tubes pre-seeded with 40 mL TM clean water (1:4 sample:dilutant). These samples were then acidified for preservation. The TM clean water was prepared by feeding water from a Milli-Q IQ 7000 purification system, through a Q-POD Element SMDS (18.2 MΩ·cm).

Sediment samples were extracted from the seabed using a stainless-steel box-corer. Box-cored sediments were sub-sampled using PVC plastic core-liners, and cores were taken well away from the steel-edge of the box to minimize risk of metal contamination. Short cores (75 mm internal

diameter, 300 mm length) and long cores (97 mm internal diameter, 500 mm length) were used to extract sediments. After collection, cores were immediately submerged into a water-bath filled with seawater from the surface of the Skagerrak. Bath water was aerated using a portable aquarium pump. Cores were stored up to 24 hours before processing. In all cases, undisturbed sediment cores with well-preserved sediment-water interfaces were selected for processing. Ambient air temperatures in the wet lab used to store and process the sediment cores ranged from 7 – 11 ºC, comparable to the 7 ºC bottom water temperature consistently measured at each sampling site.

Oxygen profiles were measured in triplicate from short sediment cores collected at each site. The profiles were measured by slowly inserting a glass micro-electrode into the sediment (Revsbech, 1983). Following oxygen measurement, the short cores were mounted into a home-built hydraulic press designed to compress sediments and force porewaters out gradually. Water was forced through air-tight iso-versinic tubing and allowed to drip into TM-clean Eppendorf tubes, pre-seeded with 50 µL concentrated TM-clean HNO_3 (~2 mL sample volume). This method is known as whole-core squeezing (WCS) (e.g. Schulz and Zabel, 2006) and is detailed in supplement 1.

A single long core from each site was sectioned for trace metal analysis. Before sectioning, bottom water was collected near the sediment-water interface with a TM-clean syringe and was filtered into 15 mL TM-clean Falcon© tubes and acidified. After bottom water sampling, cores were inserted into a sealed plastic glove bag, which was then filled with N_2 several times to produce a low-oxygen atmosphere. Desired sediment horizons were sectioned using TM clean implements, and recovered sediments were deposited in 50 mL TM clean Falcon© tubes and homogenized. After sectioning, sampling vessels were sealed and removed from the N_2 atmosphere.

To separate porewaters from sediment solids, the Falcon© tubes were immediately centrifuged at ambient air temperature for 10 minutes at 3000 RPM. Centrifuged sediment samples were transferred to a second, clean N_2 filled plastic glove bag. Three mL of porewater from each sample were extracted using TM clean implements and filtered into 15 mL TM clean Falcon© tubes. Porewater samples were acidified to 2% HNO_3 using TM-free concentrated nitric acid after removal from the N_2 atmosphere. After being separated from porewaters, wet sediment solids were sealed in their sampling vessels and then frozen. These sediments were kept frozen until analysis.

For each site, a second long core was sectioned in open air for the measurement of sediment density and water content. Sampled horizons were deposited into zip-tight bags, homogenized, and frozen until analysis.

We additionally report metal concentrations measured from suspended particulate matter (SPM) transported in five rivers (R1-R5) along the coast of Norway (fig. 1). Particulate samples from R4 and R5 are from steep rivers fed directly by mountain streams. In contrast, R1, R2, and R3 are meandering rivers representing comparably large water sheds and larger outflows into the Skagerrak (tbl. 1). These rivers were sampled between the 5th and 7th of April 2023. Between 1-25 mg of solid particulates were recovered. A complete report of the methodology used to sample these sites is available in Olesen et al. (2025).

3.2 Sample analysis

3.2.1 Solid components and sediment physical properties

Frozen sediments collected for density and water content were thawed immediately before measurement. Wet sediment aliquots were measured into pre-weighed 4 mL cut-off syringes and weighed for the calculation of density (ρ, g mL^{-1}). Water content (β, g_{Water}/g_{Total} x 100 %) was calculated as the mass-lost from sediments after drying for 24 hours, at 110 ºC. Density and water content are used to calculate porosity (φ) using equation 2:

$$\varphi = \beta \,/\, (\beta + (1 - \beta)/\rho) \qquad \text{eq. 2}$$

3.2.2 Solid metal analyses

Our sequential extraction methodology is detailed in Olesen et al. (2025). Here, we include a summary of the extraction steps. Before the first extraction, wet sediments were thawed and subsampled. Subsampled wet-sediments were first immersed in NH_4-acetate to remove exchangeable cations and easily dissolved carbonate phases (Wick et al., 2020). Following this step, Mn-oxides were targeted using hydroxylamine-hydrochloride (Neaman et al., 2004), and subsequently, Fe-(oxyhydr)oxides were targeted with dithionite (Poulton and Canfield, 2005). After

these treatments, sediments were exposed to HNO_3 to dissolve any remaining authigenic phases (e.g. Fan et al., 2021; Wu et al., 2020; Owens et al., 2017). The success of each extraction in dissolving targeted minerals is evaluated in this manuscript. Any residual matter remaining after these extractions was completely dissolved in boiling concentrated HNO_3:HF:HCl in a 3:2:1 volumetric ratio (tbl. 2). The acronyms used to identify each extraction, acid molarities, and extraction timetables are shown in table 2.

Extraction supernatants were acidified to 2 % HNO_3 and monitored for precipitation prior to analysis. No precipitation was observed. Elemental abundance was measured on a quadrupole-ICP-MS, Agilent 7900, at the University of Southern Denmark. Measurements were performed using He collision cell technology, and plasma suppression was corrected for by normalizing to an on-line addition of Scandium, Rhodium, Indium, and Iridium. Calibration standards were prepared from stock solutions and were matrix matched with extraction solutions. An additional dilution by 8x or 25x Ar gas was applied to account for high dissolved element concentrations in sample matrices. We report uncertainties as the 2se of a replicate extraction (n = 5), split from the relatively metal-poor sample S4-5.

3.2.3
Porewater, bottom water, and seawater analysis

Centrifuged porewaters, WCS extracted porewaters, seawater, and bottom-water samples were analyzed at Southern Denmark University, on an Agilent 7900 quadrupole-ICP-MS. Each sample was additionally diluted with 2% HNO_3 prior to measurement, 1:4 sample:solution. A standard curve was prepared from stock solutions using the same 2% HNO_3 matrix. Samples were further diluted immediately before ionization by the addition of 4x argon gas to promote a stable plasma stream and mitigate the risk of signal suppression due to ion precipitation on the sensor cones. Reference material NIST-1643f was analyzed with each run to evaluate reproducibility and to ensure precision. References were replicated within 20 % for V, Mn and Fe. We calculate sample uncertainties using the 2se of a replicated standard (n = 5).

3.2.4
V isotope analysis

A single-step nitric acid extraction (tbl. 2) was used to extract V from sediments for isotope analysis. This extraction has previously been used to digest the bulk of hydrogenetic and diagenetic

solid phases, including (oxyhydr)oxides and exchangeable cations, without significantly digesting solid phases transported from the upper continental crust (e.g. Fan et al., 2021; Wu et al., 2020; Owens et al., 2017). Details of the extraction are available in Olesen et al. (2025). Potential partial dissolution of the crustal background by nitric acid is evaluated in the present manuscript. Following extraction vanadium was isolated from sample matrix following previously published methods (Nielsen et al., 2019; Nielsen et al., 2011) at Woods Hole Oceanographic Institution (WHOI). The complete isolation procedure is available in supplement 2. Less than 2 % of V from each sample was lost during the isolation procedure compared to the initial extraction leachate. After V isolation, samples were analyzed on a Thermo-Finnigan Neptune MC-ICP-MS for their stable isotopic composition, reported using $\delta^{51}V$ values (eq. 1).

Isotopic compositions were calculated using standard-sample bracketing, relative to the Alfa-Aesar standard reference. Additionally, all samples were interspersed with a V reference solution from BDH chemicals, $\delta^{51}V_{BDH}$ = -1.20 ‰ (Nielsen et al., 2019; Nielsen et al., 2011; Prytulak et al., 2011; Schuth et al., 2017; Wu et al., 2016). Precision and accuracy were evaluated by assessing measurement of BDH throughout the course of mass spectrometric sessions ($\delta^{51}V_{BDH}$ = -1.22 ± 0.24 ‰, 2sd, n = 128). Reference materials USGS-SCo-1 ($\delta^{51}V$ = -0.64 ± 0.05 ‰, 2sd, n = 3) and USGS-BHVO-2 ($\delta^{51}V$ = -0.81 ± 0.07 ‰, 2sd, n = 3) processed in parallel with the samples were also analyzed. Values obtained for SCo-1 and BHVO-2 are within error of previously published values (Heard et al., 2023; Wu et al., 2020; Wu et al., 2016; Prytulak et al., 2011). Samples were measured in duplicate or, if sample volumes permitted, in triplicate, and error is reported as 2x the standard deviation (2sd) of each sample population, or as the 2sd of the BHVO population, whichever value is larger.

3.3 Treatment of sediment solid metal abundance data

Solid metal abundances liberated into each extraction solution have been converted to dry-mass concentrations. To perform this conversion, the abundance of each element in the extracted analyte was first corrected for dilution. Resulting total elemental masses measured from each analyte were then normalized to the initial dry mass of each sub-sample exposed to the sequential extraction procedure. Because wet sediments (Sed_{Wet}, g) were used in the extraction procedure, initial dry masses (Sed_{Dry}, g) were calculated using sediment water contents (β), per equation 3:

346 $$Sed_{Dry} = Sed_{Wet} * (1 - \beta)$$ eq. 3.

347 Total elemental concentrations for a given sediment sample are calculated as the sum of all
348 extraction steps.

349 Accounting for the V input from continental detritus is necessary when studying marine V cycling.
350 Vanadium is primarily delivered into the modern ocean by rivers (e.g. Nielsen, 2021), and 98.6% of
351 that V is bound in terrigenous particulates, referred to here as detritus (Oelkers et al., 2011; Viers et
352 al., 2009). As a consequence, detrital V often represents the majority of solid V accumulating in a
353 marine sediment and almost always represents a significant fraction of total V in marine sediment
354 samples (Little et al., 2025; Nielsen, 2021; Bennett and Canfield, 2020). Sediments that are almost
355 completely authigenic or biogenic are exceptions to this rule (e.g. Brumsack et al., 2006; Calvert
356 and Piper, 1984). As noted in section 2, the sediments of the Skagerrak are primarily composed by
357 detrital inputs from the North Sea and detrital inputs from the Kattegat and surrounding rivers.
358 However, there is no guarantee that detritus accumulates in the Skagerrak at a constant rate relative
359 to authigenic inputs. As such, the relative portion of detrital V in a given sample might change with
360 depth in a sediment column.

361 We have chosen to use Al-normalization to account for variations in detrital input to the sediment.
362 Aluminum normalization is commonly employed to account for continental detritus (e.g. Bennett
363 and Canfield, 2020). Rates of Al authigenesis in seawater are often small compared to detrital inputs
364 (e.g. Brumsack, 2006; Van Der Wejden, 2002). Therefore, a change in Al concentration with depth
365 in many marine sediments will be primarily controlled by the relative proportions of detrital and
366 authigenic/diagenetic input to the sediment through time. In the case that Al is converted or
367 incorporated into an authigenic clay phase (e.g. Bennett et al., 2023), Ti may instead be used to
368 evaluate detrital inputs (Brumsack et al., 2006). However, Ti concentrations are sensitive to
369 particulate sorting, such that shelf sediments in the Skagerrak are likely enriched in heavy Ti
370 bearing minerals like rutile (Brumsack et al., 2006) compared to basin sediments, meaning that the
371 element cannot be used to consistently estimate crustal inputs across the Skagerrak transect.

372 **4 Results**

373 **4.1**

374 **Physiochemistry of sediments and riverine particulates**

The density (ρ) and water-content (β) of our sediment samples (tbl. 3) are consistent with high mud contents on the slope and in the basin of the Skagerrak and high sand contents on the shelf (Diesing et al., 2021; Canfield et al., 1993a,b). Site 4 has the lowest Al concentration of all sampled sites (<4 wt. %) and the highest marine sediment Ti/Al ratios, corresponding to relatively high portions of silica sand (Canfield et al., 1993a). In comparison, S6 and S9 have Al contents exceeding 6 wt. % corresponding to higher portions of silt and clay (Canfield et al., 1993a) (tbl. 4), and S9 hosts the lowest marine sediment Ti/Al ratios. Total organic carbon (TOC) concentrations (tbl. 4) approach 3 wt. % at our basin site (S9), exceed 3 wt. % at our slope site (S6) and are less than 1 wt. % on the shelf (S4). The Al concentrations of SPM collected from the steep rivers R4 and R5 are much lower than those measured in the marine sediments while the meandering rivers R1, R2, and R3 show a range of Al concentrations comparable to the marine sediments (tbl. 4).

In our marine sediment samples, V, Mn and Fe all show increasing Al-normalized values moving from shelf to slope to basin (fig. 2). Total V/Al values are near the upper continental crust (UCC; Rudnick and Gao 2014) at S4 and are enriched at S6 and S9 (fig. 2). Total Fe/Al values are at or just below the UCC at S4, are likely enriched at S6, and are significantly enriched at S9 (fig. 2a). At S6, Fe/Al errors (2se) for each sample do encapsulate the UCC at their lower bound. Total Mn/Al values are depleted relative to the UCC in all samples from S4 and some samples at S6 (fig. 2b). The Mn/Al deplete samples from S6 were collected below 3.5 cm in the sediment column (see fig. 3). At S9, Mn/Al values in all sampled sediments are very enriched compared to UCC; there is a large spread in these values with the most intense enrichments clustering in surface sediments (compare figs. 2b and 3). Overall, and across sites, V enrichments show a linear correlation to Fe/Al and do not show a consistent linear correlation to Mn/Al (fig. 2). When compared to Fe/Al, V/Al values measured from S9 plot above a linear regression line calculated using all marine sediment samples (fig. 2a), and there are some exceptionally high V/Al values localized in the top of the sediment column at S9 (compare figs. 2b and 3).

Aluminum normalized V, Mn and Fe values measured from our riverine particulate samples plot in two distinct populations. Meandering river SPM samples R1 and R3 show V/Al enrichments relative to UCC but are less enriched in V than marine sediments from S6 and S9. Meanwhile, R1, R2, and R3 show Fe/Al enrichments comparable to marine sediments (fig. 2a). In the case of meandering rivers, Mn/Al enrichments are within range of the enrichments observed at S6 (fig. 2b) but are never depleted relative to UCC. In contrast, steep river SPM samples show very high Fe/Al enrichments relative to marine sediments and show V/Al and Mn/Al enrichments comparable to

those found at S9. However, these high enrichments are the result of relatively low Al values in steep river SPM samples (tbl. 4) rather than relatively high V, Mn, or Fe values.

The percentage of total Al, Ti, Mn, Fe, and V liberated by each extraction step from our marine sediment samples is presented in table 5. Insignificant percentages of Al, Ti, V and Fe and a minimal percentage of Mn are liberated by the ammonium-acetate extraction, intended to dissolve easily exchangeable cations (hence termed the EC step). Indeed, the EC step only liberates appreciable amounts of Mn, relative to other extraction steps, at S4 (fig. 3). All other extraction steps liberate considerable percentages (tbl. 5) and concentrations (fig. 3) of Mn, Fe, and V at all sites (fig. 3). Concentrations of Mn, Fe and V liberated from residual matter (RM) and by nitric acid (NI) primarily vary between sampling sites, while Mn, Fe, and V concentrations liberated by the hydroxylamine-hydrochloride (HH) and dithionite (DI) extractions vary dramatically between sites and across sampling depths (fig. 3). Furthermore, all Al and Ti present in our marine sediment samples was liberated by the RM and NI extraction steps (tbl. 5). For these reasons, we present the RM and NI extractions separately from the EC, HH, and DI extractions in figure 3. In the text below and throughout this publication, we generally consider RM and NI first, and then consider HH and DI, roughly in reverse order of our extraction procedure.

4.2
Correlation of Mn, Fe and V with Al liberated by the RM and NI extraction steps

The NI extraction liberated an average of 31 % of Al, and all remaining Al was dissolved by the RM extraction. In contrast, NI liberated an average of 8% of Ti, and all remaining Ti was dissolved by the RM extractions. The majority of V in our marine sediment samples was liberated with Al and Ti by the RM and NI extractions (tbl. 5, 62 ± 14 % total V). The two extractions liberate increasing concentrations of V from shelf to slope to basin. The amount of V liberated by RM is similar to NI at all depths at S4 and S6; at S9, NI liberates somewhat more V than RM in deep sediments (fig. 3). The RM and NI extractions also liberated considerable percentages of total Fe and Mn (tbl. 5). At all sampling sites, the NI extraction liberated more Mn and Fe than the RM step (fig. 3). Additionally, from shelf to basin, NI liberated an increasing concentration of Mn and Fe relative to RM (fig. 3). Across all sites and depths, concentrations of Al liberated by RM + NI correlate well to concentrations of V, Fe, and Mn liberated by RM + NI: the relevant correlation factors are 0.97, 0.97, and 0.91, for V, Fe, and Mn, respectively.

4.3

Distinct liberation of Fe and Mn by the DI and HH extraction steps

Our extraction procedure was designed to preferentially dissolve Mn-oxides using HH, and Fe-(oxyhydr)oxides using DI (tbl. 2). The potential solid-state transformation of V, Mn and Fe at reducing depths in the sediment column is discussed in section 5.3.1. Below, we compare the Mn and Fe concentrations liberated by our HH and DI extractions, respectively, to published measurements of solid Mn(IV) and Fe(III) concentrations in sediments from parallel sites sampled from the Skagerrak in 1991 (Canfield et al., 1993b), to verify that our extractions have successfully digested the intended (oxyhydr)oxide phases.

The HH extraction step liberated substantial percentages of Mn, and almost no Fe (tbl. 5). In Skagerrak samples previously analyzed for Mn speciation, Mn(IV)-oxides were most enriched in oxygen-replete portions of the sediment column and Mn concentrations increased from shelf to slope to basin (Canfield et al., 1993b). While we did not explore Mn oxidation state, our HH data showed similarly high surface Mn enrichments, and a general increase in surface Mn concentrations in transiting from the shelf to the deep basin (fig. 3). Moreover, HH extracted Mn accounts for almost all Mn extracted from deep basin sediments, which are known to host impressive concentrations of Mn-oxide (Canfield et al., 1993b; Thamdrup and Daalsgaard, 2000). Our HH extraction results are therefore consistent with the targeted dissolution of Mn-oxides, particularly in the Mn-oxide enriched deep basin.

Conversely, the DI extraction step liberated 30 (± 10, 1sd) % of total Fe, while only liberating 5 (± 2, 1sd) % of total Mn across the sites on average (tbl. 5). Concentrations of Fe liberated by the DI step increase from shelf to slope to basin (fig. 3), reproducing the Fe(III)-(oxyhydr)oxide enrichment trends reported by Canfield et al. (1993b). Our DI extraction results are therefore consistent with the targeted dissolution of Fe-(oxyhydr)oxides.

4.4

Diagenesis of V, Mn, and Fe in Skagerrak sediments

Measurable concentrations of dissolved oxygen are present at the top of each sediment column, diffusing downwards from the sediment water interface (SWI). Dissolved oxygen falls below detectable concentrations at 1.8 cm at S9, 1.3 cm at S6, and 0.8 cm at S4 (fig. 4), defined as the oxygen depletion depth (ODD). Above the ODD, porewater Mn is dilute relative to deeper depths at S9 and S6 and decreases in concentration approaching the sediment water interface (SWI) at S4

(fig. 4). Sediment Mn concentrations peak at the ODD at S4 and S9, and peak above the ODD, at the SWI, at S6 (fig. 3). In contrast, porewater Fe is relatively absent above the ODD (fig. 4), and sediment Fe concentrations are relatively irresponsive to the ODD when compared to Mn. Indeed, the only discernable responses are a small depletion in DI liberated Fe (Fe_{DI}) in the surface sediments of S4, and a relatively small enrichment of Fe_{DI} in the surface sediments of S9, relative to sediments immediately below the ODD (fig. 3). In all centrifuged porewater samples, dissolved V never falls below 4 $\mu g\ L^{-1}$, a higher concentration than that sampled from bottom water and seawater (fig. 4). In contrast, V concentrations in WCS extracted porewaters (red dots) consistently decrease approaching the SWI (fig. 4). Concentration of V in sediment above the ODD are depleted in V S4, are invariant at S6, and are enriched at S9, relative to sediments below the ODD (fig. 3). Sediment V depletion/enrichment trends above the ODD are dependent on a mixture of extractions at S4 and are primarily dependent on HH liberated V (V_{HH}) concentrations at S9 (fig. 3).

Below the ODD, our porewater results generally reproduce expected trends for Fe and Mn reduction (see Canfield et al., 1993b; Lovley, 1991; Froelich et al., 1979) at all marine sampling sites. Moving from shelf to slope to basin, peak porewater Mn concentrations increase (fig. 4) – reflecting the increased importance of Mn-reduction to carbon oxidation in this transect (Canfield et al., 1993b). Conversely, the decrease in pore water Fe concentrations in transiting from shelf to deep basin reflects the decreased importance of Fe-reduction (Canfield et al., 1993b). Porewater Fe peaks are at the same depth (S4) or below (S6 and S9) porewater Mn peaks.

The accumulation of V in porewaters below the ODD shows an inconsistent relationship to patterns of Mn and Fe dissolution across sites (fig. 4). Centrifuged porewater V concentrations always increase below the ODD, and the depth of this increase deepens from basin to slope to shelf (fig. 4). At S4, there is a major porewater V peak below the depth of Fe depletion from porewaters, and below the depth where porewater Mn reaches stable low concentrations (fig. 4). Additionally, at S4, there is a minor porewater V peak just below peaks in porewater Fe and Mn. At S6, porewater V shows an increasing concentration with depth below the porewater Fe peak (fig. 4). At S9, porewater V peaks above the porewater Mn peak (figs. 4). Above this peak, porewater V reaches its background concentration somewhat below the ODD (fig. 4).

The depth that porewater Mn peaks in a given sediment generally correlates to the depth exhibiting a significant reduction in the rate of change of Mn_{HH} (figs. 3 and 4), indicating the lower depth where Mn_{HH} dissolution evidently supports Mn reduction. At S9, Mn_{HH} concentrations show an

additional secondary minimum deeper in the sediment column (ca 12 cm) (fig. 3). Below these minima, at S6 and S9, Mn_{HH} concentrations reach a negligibly small fraction compared to top sediments. Sediment V_{HH} trends show variable relationship with Mn_{HH} trends across sites. At S4, V_{HH} and Mn_{HH} concentrations are relatively invariant above the ODD, but V_{HH} is higher and Mn_{HH} is lower below the ODD relative to top sediments. At S6, V_{HH} is depleted, relative to deeper sediments, above the Mn_{HH} minimum. At S9, V_{HH} decreases with Mn_{HH} down to the primary Mn_{HH} minimum; V_{HH} maintains an invariant and appreciable concentration below this depth. The depth of the V_{HH} minimum (fig. 3) correlates to the V porewater peak (fig. 4).

With regard to Fe_{DI}, concentrations are highest at all sites in top sediments and then decrease to a lower concentration below, and this low concentration is sustained to the deepest measured depth. This decrease occurs at 3.5 cm, 7 cm, and 13 cm at S4, S6, and S9 respectively. At all sites, porewater Fe reaches its highest measured concentration below this Fe_{DI} depletion depth. There is an anomalous, secondary porewater Fe peak above the Mn peak at S9 (fig. 4), which correlates to a local minima in Fe_{DI} concentrations (fig. 3). However, neither the Fe_{DI} minima nor the relatively high porewater Fe concentrations are sustained with increasing depth (figs. 3 and 4). Concentrations of V_{DI} and Fe_{DI} are well correlated ($R = 0.99$) across all marine sediment samples (figs. 3, 5), mimicking the V/Al and Fe/Al enrichment trend reported in section 4.1 (fig. 2a).

Concentrations of V and Fe liberated by both HH + DI (V_{HH+DI} and Fe_{HH+DI}, respectively) plot near the V_{DI}/Fe_{DI} trendline at S4 and S6 (fig. 5). In contrast, V_{HH+DI}/Fe_{HH+DI} from S9 plots above the V_{DI}/Fe_{DI} trend, primarily due to the contribution of V_{HH} (fig. 5). Riverine SPM has lower V_{DI}/Fe_{DI} and V_{HH+DI}/Fe_{HH+DI} ratios than marine sediments (fig. 5). Excluding SPM from the R5, sediment samples at S6 host a higher V_{HH+DI} than riverine SPM; S9 is always more concentrated in V_{HH+DI} than riverine SPM. In contrast, SPM from R1 and R2 hosts a higher V_{HH+DI} concentration than samples from S4.

4.5
$\delta^{51}V$ composition of single-step nitric acid leachate

A single-step nitric acid leach (NI*, tbl. 2) was used to liberate V from solid sediment samples for isotopic analysis. The NI* extraction should, in principle, dissolve the same concentrations of V (V_{NI*}) and Al (Al_{NI*}) when compared to the sum of our own nitric extraction, together with the preceding extraction steps, namely NI+HH+DI ($\sum$NI) (tbl. 2). The $\sum$NI for V and Al are referred to as $V_{\sum NI}$ and $Al_{\sum NI}$. Generally, V_{NI*} and $V_{\sum NI}$ concentrations are similar (fig. 6a), except for 5

samples at S4 that show unreasonably high V_{NI*} contents; indeed, V_{NI*} is higher than V_{Total} in these samples. The potential causes of this anomaly are addressed in supplement 3. Concentrations of V_{NI*} and $V_{\sum NI}$ from the marine sediment samples are cross plotted with corresponding Al_{NI*} and $Al_{\sum NI}$ concentrations in fig. 5. In general, the NI* extraction results in a larger spread of V and Al concentrations than the ∑NI extractions, more so at S6 than at S9. Per site, V_{NI*}/Al_{NI*} ratios are consistently comparable to $V_{\sum NI}/Al_{\sum NI}$ ratios, save for one sample with a relatively high V_{NI*}/Al_{NI*} at S4 and a cluster of relatively high $V_{\sum NI}/Al_{\sum NI}$ values at S9 (fig. 6b).

Figure 7a shows depth distributed $\delta^{51}V$ values measured from NI* treated samples ($\delta^{51}V_{NI*}$), and fig. 7b shows the mean $\delta^{51}V_{NI*}$ calculated for S6 and S9. Mean $\delta^{51}V_{NI*}$ values calculated for S4 excluding and including the anomalously concentrated samples are available in supplement 3. Regardless of whether the anomalous samples at S4 are considered or not, the $\delta^{51}V_{NI*}$ average is highest at S9 compared to other Skagerrak sites (fig. 7b). Moreover, the top 4 samples at S9 exhibit a $\delta^{51}V_{NI*}$ value significantly higher than the typical oxic sediment sink ($\delta^{51}V_{Oxic,}$ fig. 7a). Only one other sample, collected from S4, shows a significantly high $\delta^{51}V_{NI*}$ value relative to $\delta^{51}V_{Oxic}$ (fig. 7a); this value was measured from the sample with the anomalously high V_{NI*}/Al_{NI*} ratio mentioned above (fig. 6b).

5 Discussion

Vanadium at each of our sampling sites shows a variable relationship to Fe/Mn cycling, both at a regional scale and as diagenesis proceeds with increasing depth into the sediment column. As a consistent trend, concentrations of V, Mn and Fe in Skagerrak sediments show increasing enrichments moving from shelf to slope to basin (fig. 2), such that V enrichments are higher on the slope and much higher in the basin than is typical for oxic sediment sinks and the UCC (section 1). We also note that a portion of V is remobilized in each of the sediment columns owing, most likely, to early Fe and Mn diagenesis (fig. 3). However, each site shows distinct patterns of coupling between V and Fe/Mn diagenesis (figs. 3, 4). In what follows, we will explore the authigenic and diagenetic processes that control the solid concentration (V_{Sed}) and isotopic composition ($\delta^{51}V_{NI*}$) of V in Skagerrak sediments.

5.1 Accounting for detrital and authigenic V inputs

About 98.6 % of V delivered into the modern ocean is bound by detrital particulates (Oelkers et al., 2011; Viers et al., 2009; also see section 3.3). As a consequence, small enrichments of V in marine

sediments can have a considerable impact on models of V cycling, and multi-fold enrichments imply relatively high proportions of authigenic vanadium input from seawater (e.g. Bennett and Canfield, 2020). Likewise, our understanding of V cycling in any given sediment is sensitive to misestimations in detrital inputs and is particularly sensitive to the detrital reference chosen. For example, North American soils (Cole et al., 2017), post-Archean (Taylor and McLennan, 1985) and modern shales (Turekian and Wedepohl, 1961), and the average upper continental crust (UCC; Rudnick and Gao, 2014) each host different average concentrations of V and Al, with significantly different V/Al ratios. Below, we carefully consider how detritus contributes to V_{Sed} and $\delta^{51}V_{NI*}$ in the sediments of the Skagerrak, taking these uncertainties into account.

Nitric acid extractions are frequently used to isolate authigenic phases for isotope measurements (e.g. Heard et al., 2023; Fan et al., 2021; Wu et al., 2020). In OCM sediments previously treated with the nitric acid extraction, less than 10 % of total Al was liberated by nitric acid (Wu et al., 2020), a result consistent with the minimal dissolution of detrital aluminosilicate mineral phases. On average, more than 30% of the total Al concentration in our sediment samples was liberated by both NI (tbl. 5, fig. 6) and NI* (fig. 6). This relatively high percentage cannot be easily explained unless our NI and NI* extractions have dissolved a significant portion of aluminosilicate minerals in Skagerrak sediments. In contrast, the NI and NI* extraction only liberated 8 % of total Ti, which preferentially accumulates in heavy aluminosilicate minerals like rutile (Brumsack et al., 2006). We therefore suspect that the high Al_{NI} and Al_{NI*} values result from dissolution of clay minerals, e.g. illite (Olesen et al. 2025), that are more prone to dissolution than heavier aluminosilicate minerals. We also note that Al can accumulate in authigenic clay phases, while Ti should not (Brumsack et al., 2006). It is therefore possible that some V-hosting clays are authigenic in origin, although it is unclear what fraction of the clay minerals in Skagerrak sediments have formed this way (Olesen et al., 2025).

While V hosted by clay minerals may be terrigenous (e.g. Nielsen, 2021; Oelkers et al., 2011), V may also adsorb onto detrital clays in seawater and sediments (Lu et al., 2021; Zhu et al., 2018) or incorporate into diagenetically altered phyllosilicate minerals (Bennett et al., 2023). In such cases, NI liberated V would be strongly coupled to detrital Al concentrations despite being authigenic in origin. Therefore, even if V liberated by NI is exclusively bound by detrital clays, an unknown fraction could be authigenic. Consequently, the size of the authigenic V pool needs to be further interpreted independent of our sequential extractions.

5.1.1 Verifying the authigenic origin of V liberated by HH and DI from the sediments of the Skagerrak

To better evaluate the likely contribution of authigenic processes to V_{Sed}, $V_{\sum NI}$, and V_{NI*}, we compare our sequentially extracted V concentrations to an estimate of V concentrations in excess (termed V_{XS}) of the V likely delivered by a given crustal reference (termed $V_{Detrital}$) (e.g. Brumsack, 2006). Here, V_{XS} is estimated relative to the average upper continental crust, which hosts a V/Al ratio (V/Al_{UCC}) of 11.9 ± 1.9 x 10^{-4} (1 sd) (Rudnick and Gao, 2014). To calculate V_{XS}, we assume that all Al accumulating in the sediments of the Skagerrak (Al_{Sed}) is detrital (section 3.3) and that V/Al ratios in the detrital fraction within Skagerrak sediments resembles the UCC, as shown in equation 4:

$$V_{XS} = V_{Sed} - Al_{Sed} * \left(\frac{V}{Al}\right)_{UCC} \quad \text{eq. 4.}$$

The V_{XS} for each marine sediment sample have been compiled, per site, as violin plots in figure 8. The potential error associated with this analysis is calculated to the first standard deviation, considering the range of values in our own sample set and the upper continental crust (Rudnick and Gao, 2014). To ensure that UCC is a reasonable proxy for detritus accumulating in the sediments of the Skagerrak, we also calculate and present V_{XS} for SPM sampled from meandering rivers R1, R2, and R3, respectively. Although local riverine SPM represents a likely minority of detritus accumulating in the sediments of the Skagerrak (section 2), its similarity or dissimilarity to the UCC (V_{XS} = 0) allows us to better evaluate the possibility that local detrital inflows to Skagerrak sediments deviate from UCC. We do not present V_{XS} for SPM sampled from steep rivers R4 and R5, because total Al concentrations are too low relative to other samples (tbl. 4) to apply equation 2 confidently (see Brumsack, 2006).

Concentrations of V_{XS} increase from shelf to slope to basin (fig. 8), such that the slope and deep basin of the Skagerrak cannot be accounted for by detritus similar to UCC, or by detritus similar to SPM in local meandering rivers. The V_{XS} concentrations we estimate at S6 and S9 are within range of V_{HH+DI} concentrations measured from the two sites (fig. 8), and depth distributions of V_{XS} at these sites mimic V_{HH+DI} depth distributions (fig. 9). The mean V_{XS} value is always a little higher than the concentration of V_{HH+DI} measured from our samples. Therefore, although V_{HH+DI} appears to account for the majority of V_{XS} on the slope and in the basin of the Skagerrak, our V_{XS} estimates are consistent with potential authigenic V accumulation on NI extractable clays. Still, distributions of

V_{HH+DI} appear to exert a primary control on distributions of authigenic V in the sediment column. If clays are also hosting authigenic V in the sediments of the Skagerrak, that authigenic V must either mimic the distribution of HH+DI extractable phases or must represent a small portion of authigenic V, relative to HH and DI extractable mineral phases, namely Mn- and Fe- (oxyhydr)oxide.

In contrast, V_{XS} concentrations estimated for S4 can potentially be explained by detrital inputs. The mean of V_{XS} values calculated for S4 plots below R1 and R2, such that V_{XS} at the site may, in part, actually be the result of a regionally high detrital background. Notably, V_{HH+DI} concentrations at S4 exceed our V_{XS} estimates (fig. 8), which implies an authigenic component. However, V_{HH+DI} at S4 is comparable to V_{HH+DI} from SPM in nearby Norwegian rivers (fig. 8), such that authigenesis in rivers may explain the V_{HH+DI} concentrations at S4 (supplement 4).

5.1.2

Estimating the contribution of authigenic and detrital V to $\delta^{51}V_{NI*}$

When considering our isotope extractions, the mean of V_{XS} and V_{HH+DI} consistently plots below V_{NI*} at all sites (fig. 8). In other words, $V_{Detrital}$ may contribute to our $\delta^{51}V_{NI*}$ values. Assuming that V_{XS} approximates the concentration of ocean-authigenic V in our sediments, the likely portion of authigenic V contributing to the V_{NI*} pool can be estimated as V_{XS}/V_{NI*}. The value of V_{XS}/V_{NI*} is compiled for each site in table 6. At S4, the authigenic fraction of samples impacted by the V_{NI*} anomaly described in section 4.4 is instead calculated as $V_{XS}/V_{\sum NI}$, on the grounds that $V_{\sum NI} \sim V_{NI*}$ in all other samples (fig. 6).

Based on the above analysis, it is possible to estimate the isotopic composition of V_{XS} ($\delta^{51}V_{XS}$), assuming that V_{XS} and $V_{Detrital}$ are the only components contributing to V_{NI*}. In this case, $\delta^{51}V_{NI*}$ is the mass-balanced product of $\delta^{51}V_{XS}$ and the isotopic composition of $V_{Detrital}$ ($\delta^{51}V_{Detrtial}$) (eq. 6):

$$\delta^{51}V_{NI*} = \left(\frac{1-V_{XS}}{V_{NI*}}\right) * \delta^{51}V_{Detrital} + \left(\frac{V_{XS}}{V_{NI*}}\right) * \delta^{51}V_{XS} \quad \text{eq. 6.}$$

This mass-balance can be reorganized to solve for $\delta^{51}V_{XS}$ (eq. 6a):

$$\delta^{51}V_{XS} = \left[\delta^{51}V_{NI*} - \left(\frac{1-V_{XS}}{V_{NI*}}\right) * \delta^{51}V_{Detrital}\right] / \left(\frac{V_{XS}}{V_{NI*}}\right) \quad \text{eq. 6a.}$$

We have measured V_{NI*} (fig. 5) and $\delta^{51}V_{NI*}$ (fig. 6) and have estimated V_{XS} and $V_{Detrital}$ (eq. 4). Since we have not measured $\delta^{51}V_{Detrital}$ in our own system, we adopt the $\delta^{51}V_{Detrital}$ of riverine suspended particulates compiled by Schuth et al. (2019). The results of our isotopic corrections for

S6 and S9 are presented in figure 10. The rationale for excluding S4 from this figure is presented below.

We find that $\delta^{51}V_{XS}$ at S9 does not significantly deviate from $\delta^{51}V_{NI*}$ (fig. 10a,b), a consequence of the high authigenic contribution to V_{NI*} estimated for the site (tbl. 6). At S6, $\delta^{51}V_{XS}$ is more sensitive to variations in both V_{XS}/V_{NI*} and $\delta^{51}V_{NI*}$. For example, the 2nd and 4th samples from the SWI at S6 show a remarkably low $\delta^{51}V_{XS}$ compared to other depths at the site (fig. 10a). This result is an artefact of our mass-balance approach. For reference, V_{XS}/V_{NI*} is 0.70, 0.63, 0.72, and 0.49 for the 1st, 2nd, 3rd, and 4th sample from the SWI at S6, respectively. Furthermore, the 2nd and 4th sample have the lowest $\delta^{51}V_{NI*}$ values in the S6 data set, not taking sample error into account. In combination, the values summarized above produce very low apparent $\delta^{51}V_{XS}$ values at the 2nd and 4th depth from the SWI for S6 when using eq. 6a. Excluding these two anomalously low values, $\delta^{51}V_{XS}$ at S6 is always comfortably in the range expected for sediments depositing beneath oxic waters ($\delta^{51}V_{Oxic}$; Wu et al., 2020). The errors highlighted above for S6 are more extreme for S4. Average authigenic V_{XS}/V_{NI*} are 5-fold lower in the top sediments of S4 than in the sediments of S6 (tbl. 6). Consequently, any errors associated with V_{XS} will be amplified compared to S6 when estimating $\delta^{51}V_{XS}$. Problematically, average V_{XS} is smaller than its associated error range at S4 (fig. 8). Consequently, any $\delta^{51}V_{XS}$ results obtained for S4 using eq. 6 cannot be considered accurate. Generally, when V_{XS} concentration are low relative to detritus, it is not possible to disentangle authigenic signals from detrital signals using the NI extraction (Wu et al., 2020).

We conclude that authigenesis is responsible for the relatively high $\delta^{51}V_{NI*}$ average observed at S9, compared to previously measured $\delta^{51}V_{NI*}$ values from other OCM sites (Wu et al., 2020). While we are more unsure of $\delta^{51}V_{XS}$ values at S6, they can conceivably be accounted for using typical fractionation effects expected to occur in oxic seawater (Wu et al., 2020; Wu et al., 2015). For S4, $\delta^{51}V_{NI*}$ and $\delta^{51}V_{XS}$ values may or may not be authigenic in origin, and we are not able to distinguish between the two possibilities. Notably, the deepest V_{XS}/V_{NI*} at S4 exceed 40 % on average (tbl. 6). Likewise, the deepest $\delta^{51}V_{NI*}$ values at S4 are identical to or lower than $\delta^{51}V_{Oxic}$ (fig. 7). Based on these observations, we cautiously propose that authigenic V buried in the sediments on the shelf of the Skagerrak likely reproduces the $\delta^{51}V$ of typical oxic inputs.

5.2 Comparing the rate of V sequestration and efflux in the Skagerrak to established V sinks

Whole-core-squeezed porewater profiles suggest that V also effluxes from all of our sediment sites (fig. 4). Although the WCS profiles do not wholly conform to the centrifuged porewater trends in the shallow sediments of S4 and S6, V efflux from porewaters is necessitated by the relatively low concentration of V in overlying bottom waters and seawater compared to the pore water (fig. 4). Indeed, V is already known to efflux from reducing OCM sediments with substantial Fe/Mn-dissimilation near the SWI (Morford et al., 2005; Morford and Emerson, 1999). Depending on the magnitude of that efflux, OCM sediments may even constitute a substantial source of V to overlying seawater (Morford and Emerson, 1999). Below, we quantify the balance between V efflux and sequestration at each of our sampling sites to understand: 1) if V effluxes upslope are an important source of V to the basin of the Skagerrak and 2) directly compare rates of V sequestration in the basin of the Skagerrak to established V sinks.

The efflux rate of dissolved V (V_{Efflux} Rate; μg cm^{-2} yr^{-1}) from our sediment sites (eq. 7) can be calculated using Fick's 1st law of diffusion (pr. Scholz et al., 2011). Efflux is assigned as a positive value, as it supplies V to the ocean.

$$V_{Efflux}\ Rate = \varphi * D_{sed} * d[V]/dZ \qquad \text{eq. 7}$$

This equation estimates the rate of V diffusion from sediments by multiplying the the slope of dissolved vanadium's diffusion out of the sediment (d[V]/dZ; μg L^{-1} cm^{-1}) to a porosity (φ) adjusted sediment-adjusted coefficient (D_{Sed}, cm^2 s^{-1}). We calculate d[V]/dZ by running a linear regression using whole core squeezed V porewater concentrations (fig. 2b). The slope of this linear regression (tbl. 7) is multiplied by the diffusion coefficient of molybdate (D_{SW}, 10^{-6} cm^2 s^{-1}; Li and Gregory, 1974) (tbl. 7) and φ (tbl. 3) to calculate V_{Efflux} Rate (tbl. 8). The reported V_{Efflux} error is proportional to the 95 % confidence interval of d[V]/dZ. Following convention (Wang et al. 2019, Scholz et al. 2011, Emerson and Huested 1991), we have selected molybdate as an analogue for vanadate in lieu of experimental measurements of V diffusivity. We adjust the diffusion co-efficient of molybdate to sediment tortuosity ($1 - \ln(\varphi^2)$ pr. Boudreau, 1996) (eq. 7a) and bottom water temperatures (7b) to estimate D_{Sed} (tbl. 6).

$$D_{sed} = \frac{D_{SW(T\,^\circ C)}}{1-\ln(\varphi^2)} \qquad \text{eq. 7a}$$

$$D_{SW(T\,^\circ C)} = D_{SW(0\,^\circ C)} + \frac{T}{25} * \left(D_{SW(25\,^\circ C)} - D_{SW(0\,^\circ C)}\right) \qquad \text{eq. 7b}$$

The rate of V sequestration from seawater ($V_{Seq.}$ Rate) is calculated for each site by multiplying wet-sediment V_{XS} concentrations by site specific sedimentation rates (Sed. Rate, cm yr^{-1}) modeled for

711 the Skagerrak seafloor by Diesing et al. (2021) (tbl. 7) (eq. 8). Sequestration is assigned a negative
712 value, as it removes V from the ocean.

713 $$V_{Seq.}\ Rate\ = -\rho * (1 - \beta) * Sed_{Rate} * \mathrm{V_{XS}}\ min \qquad \text{eq. 8}$$

714 To avoid errors related to compaction, we adjust our dry sediment concentrations to wet sediment
715 concentrations by multiplying them by the average density (ρ; g cm^{-3}) and solid mass fraction (1 –
716 β) of Skagerrak top sediments (tbl. 3), rather than using parameters from deep sediments. We use
717 minimum V_{XS} concentrations sampled below the depth of Fe/Mn-(oxyhydr)oxide depletion (fig. 9)
718 to estimate the concentration of V in sediments which has been sequestered from seawater. This
719 approach means that we do not use V_{XS} concentrations that may be enriched by diagenesis. Because
720 we are uncertain of the V_{XS} contents at S4 (fig. 8), we do not calculate a $V_{Seq.}$ rate at the site.

721 Rates of V_{Efflux} and V_{Seq} are compared to each other in table 8. Rates of V_{Seq} (tbl. 8) have a high
722 uncertainty due to the high variability of sedimentation measured across the slope and basin of the
723 Skagerrak (Diesing et al., 2021). The sedimentation rates previously referenced by Canfield et al.
724 (1993b) to calculate metal influxes into the basin of the Skagerrak are 0.1 – 0.2 cm yr^{-1}, lower than
725 but within the error range of the sedimentation rates we have chosen to reference in the present
726 publication.

727 Using average rates, the sequestration of V exceeds the efflux of V at S6 and S9 by 40x and 120x,
728 respectively. In other words, V_{Efflux} is negligible compared to $V_{Seq.}$ in the basin of the Skagerrak.
729 Average V_{Seq} Rates calculated at S6 and S9 are remarkably high compared to rates previously
730 measured on the OCM, and in fact exceed rates measured for sediments underlying oxygen
731 minimum zones (OMZs) (tbl. 8). However, these average rates may be unrealistic considering the
732 high uncertainty associated with Sed. Rate in our calculations (tbl. 8). If we instead consider the
733 V_{Seq} Rates at the lowest end of the error range (tbl. 8), the basin of the Skagerrak still exhibits a
734 $V_{Seq.}$ Rate at least 10x higher than the V efflux rate, and about 10x and 1.5x higher than the upper
735 error range of the V_{Seq}. Rate compiled by Nielsen et al. (2021) for OCMs and OMZs, respectively.

736 Rates of V_{Efflux} at S4 are an order of magnitude lower than those calculated from S6 and S9 (tbl. 8),
737 such that the shelf is unlikely to be an important source of V to the basin of the Skagerrak. This
738 result highlights that diagenetic V cycling between Skagerrak sites is unlikely to supply the V
739 enrichments observed in basin sediments. Instead, this V must be either: 1) supplied from sources
740 outside of the Skagerrak, 2) adsorbed from seawater overlying the Skagerrak seaway, or 3) related
741 to diagenetic V cycling within individual sediment columns.

5.3

Distinct roles of Fe-(oxyhdyr)oxide and Mn-oxide for enriching V in the Skagerrak

Concentrations of V_{XS} (fig. 8), V_{Seq}. Rates (tbl. 8), and $\delta^{51}V_{XS}$ values (fig. 10b) are notably elevated in the basin of the Skagerrak compared to the slope. This is particularly true for top sediments at S9, the only sediments that host $\delta^{51}V_{XS}$ values significantly higher than $\delta^{51}V_{Oxic}$ (fig. 10a). Therefore, V geochemical signals preserved in the basin of the Skagerrak are likely impacted by processes absent on the slope. Vanadium authigenesis can occur both in seawater and/or during early diagenesis within sediments. Understanding which processes are responsible for the unique V composition of Skagerrak basin sediments requires careful comparison of vanadium's solid phase speciation to patterns of enrichment and diagenesis across sampling sites.

As a common feature across sampling sites, our marine sediment samples show consistent correlations between V_{DI} and Fe_{DI} concentrations (fig. 5) and V/Al and Fe/Al enrichments (fig. 2a). Furthermore, V_{DI} concentrations at S6 and S9 account for the majority of the V_{XS} pool (fig. 9, tbl. 6) and a substantial portion of the V_{Total} pool (fig. 3). Given that Fe_{DI} corresponds to Fe-(oxyhydr)oxide distributions in the sediment (section 4.3), the covariance between V_{DI} and Fe_{DI}, and the fact that V_{DI} represents the majority of the authigenic component, supports the hypothesis that V-Fe-(oxyhydr)oxides are a major removal pathway for V dissolved in Skagerrak seawater.

However, at S9, there is additional V enrichment associated with the V_{HH} step that targets Mn-oxides (fig. 5). Therefore, at S9, both Fe and Mn-(oxyhdr)oxides appear to sequester V, supplying a more efficient V sink than at S6. The increased efficiency of V sequestration at S9 is also observed when V/Fe_{Total} trends are considered (fig. 11), where sediments plot above a ratio common to S4 and S6. As discussed above, Mn-oxides hyper-accumulate in the sediments of S9 (fig. 3a, Olesen et al. 2025, Canfield 1993b) and we therefore argue that V-Mn-oxide adsorption in seawater is a potential additional source supplying additional V_{XS} to the site, beyond what is supplied in association with Fe.

5.3.1

Sensitivity of V_{XS} concentrations to diagenesis

With sediment depth, the (oxyhydr)oxides that may have initially adsorbed V from seawater are completely or partially dissolved (figs. 3, 4). This dissolution does not impact Mn-oxides and Fe-(oxyhydr)oxides to the same degree. For example, Mn_{HH} approaches zero in sediments below ca. 4-6 cm at S6 and 12 cm at S9 (fig. 3), while Fe_{DI} persists to the deepest depth measured in the

sediment column. These results are consistent with the complete reductive dissolution of Mn-oxides at reducing depths in Skagerrak sediments. To explain the Fe_{DI} trends, Fe-(oxyhydr)oxides either only partially dissolve and/or Fe accumulates in dithionite dissolvable reduced mineral phases with increasing depth into Skagerrak sediments. Parallel sediments sampled near S6 host substantial concentrations of Fe^{2+} bearing sulfide at reducing depths (Canfield et al., 1993b), which may be dissolved by our dithionite extraction (Poulton and Canfield, 2005). Parallel sediments from S9 hosted very little acid volatile Fe sulfide that might also be included in the dithionite extraction (Canfield et al., 1993b), such that we can be more certain that Fe-(oxyhydr)oxides persist with increasing depth at the site.

Based on these observations, V adsorption in seawater cannot be the only factor that controls the distribution of authigenic V_{XS} in the sediment column. Some V_{HH} persists even below the depths that Mn-oxide has dissolved into sediment porewaters (fig 3), such that V in the deep sediments of the Skagerrak is decoupled from Mn. At these depths, V_{HH} must be hosted by another mineral phase, for example diagenetic carbonates (Breit and Wanty, 1991), which are known to form in Skagerrak sediments (Rajendran et al., 1992) and are dissolved by the HH extraction (Neamann et al., 2004), or non-specific silicate phases. In contrast, V_{DI} distributions always mimic Fe_{DI} distributions (fig. 3, fig. 5), such that V likely mirrors the fate of Fe-(oxyhydr)oxides in Skagerrak sediments, whether they persist or are reduced into diagenetic sulfides.

These variable dynamics of V-Mn and V-Fe coupling lead to distinct patterns of V-cycling within slope and basin sediments. At S6, V cycling in sediments is controlled by Fe-(oxyhydr)oxides. At this site, authigenic V is predominantly bound to Fe-(oxyhydr)oxides in the surface sediments (fig. 3, 9) and is released to the porewaters as these phases are reduced (fig. 4). Both dissolved V and Fe^{2+} diffuse to the sediment surface (fig. 4), and reform again as the Fe^{2+} is re-oxidized to Fe-(oxyhydr)oxides, allowing V re-adsorption. For S9, the situation is similar, but instead of Fe, V dynamics are controlled by Mn diagenesis (figs. 3 and 4).

In adsorption experiments, Mn-oxides are generally less prone to adsorbing V than Fe-(oxyhydr)oxides, particularly (Abernathy et al., 2022). The dominance of Fe-(oxyhydr)oxides in controlling V diagenesis at S6 is owing to their high concentrations and low concentrations of Mn oxides (Figure 3). At S9, Mn-oxides are likely most important in controlling V diagenesis owing to their unusually high concentrations. Additionally, Fe diagenesis at S9 is subdued due to the high Mn-oxide levels (Canfield et al., 1993b), potentially restricting the formation of fresh, V reactive

Fe-mineral phases (Abernathy et al., 2022). As stated above, there appears to be a stable pool of Fe (oxyhydr)oxide-associated V at S9 that persists with depth. Because Mn dominates V diagenesis at S9, this V-Fe-(oxyhydr)oxide pool likely precipitated in seawater. Even when Fe reduction does occur in the deeper sediments of S9 (ca. 12 cm), it does not result in substantial release of V to the porewaters (fig. 4). This apparent contradiction might be explained if the Fe reduction apparent from porewater Fe^{2+} profiles (fig. 4), only reduced a small amount of the available Fe-(oxyhydr)oxides, allowing V association with the residual (oxyhydr)oxides to persist. Fresh, diagenetic Fe-(oxyhydr)oxides would be more prone to dissolution, and more prone to hosting V that may be released to porewaters.

The prominent role of diagenesis in coupling V and Mn in the basin of S9 is driven by high Mn-oxide concentrations. This does not necessarily mean that Mn-oxides are not an important V sink at S9, or at other sites on the OCM. Our results do, however, predict that V enrichments above those typically observed in OCM sediments are driven primarily by Mn-oxide deposition only if there is a source of abundant and reactive Mn-oxides capable of competing with Fe-(oxyhydr)oxides (Abernathy et al., 2022) as a host for V in seawater.

5.3.2 Sensitivity of V to supplies of Fe-(oxyhydr)oxides and Mn-oxides into the basin sediments of the Skagerrak

We have identified two distinct sinks enriching V in the sediments of the Skagerrak. One which adsorbs V_{DI} with consistent efficiency at all sites – likely composed of Fe-(oxyhydr)oxide minerals, and one which adsorbs V_{HH} with unique efficiency at S9 – likely composed of Mn-oxide minerals (fig. 12). In the previous sub-section, we highlight that the V_{HH} pool at S9 is, at least partially, composed by diagenetic V-Mn-oxide precipitating in the sediment column. However, diagenetic redistribution of V internal to the sediment column at S9 fails to explain why the entire sampled sediment column exhibits high V_{HH+DI}/Fe_{HH+DI} (fig. 5), V_{Total}/Fe_{Total} (fig. 11), and V_{Total}/Al_{Total} (fig. 2) values relative to S4 and S6. We propose here that basin dependent processes of particulate sorting and diagenetic Mn cycling between sites can explain the observed V enrichment trends (fig. 12).

In the case of the consistent V-sink, basinal hydrography may enhance V enrichments through processes of particulate sorting. Detritus in the basin of the Skagerrak is almost entirely composed of clay and silt sized particulates (Diesing et al., 2022, Canfield et al., 1993a) and particles of this

size make up the majority of detritus in the whole Skagerrak region (Van Weering et al., 1993). Generally, Fe enrichments increase as the concentration of Al-bearing fine particulates increase (fig. 2a). Indeed, Fe_{DI} distributions are very similar to Fe_{NI} distributions in the sediment (fig. 3), supporting the interpretation that Fe-(oxyhydr)oxides and clays share the same pattern of deposition in the Skagerrak region. This trend makes sense if both components, and their respective V-pools, are transported into the Skagerrak region by the same processes. Danielsson et al. (1999) found that sediment concentration of Fe and the trace metals Zn, Cd, Co, Cu and Pb consistently co-varied across the entire Kattegat and Skagerrak region. They hypothesized that fine grained Fe-(oxyhydr)oxides flocculated along the coast, near fresh-water inputs feeding the North Sea and Skagerrak, incorporating trace metals upon their formation outside of the Skagerrak basin. Our own analysis of Fe-diagenesis in the region supports this hypothesis. None of our sites show evidence for Fe efflux from the sediment column (fig. 4b) which might feed fresh Fe-(oxyhydr)oxide precipitation in overlying seawater, a result concordant with existing studies on Fe cycling in the Skagerrak (Siems et al., 2025; Danielsson et al., 1999; Canfield et al., 1993a,b; Rajendran et al., 1992).

Based on the above analysis, we propose that a consistent assemblage of allochthonous Fe-(oxyhydr)oxide minerals forming outside the Skagerrak sinks into the waters encapsulated by the basin (fig. 12), either as fine particulates transported similarly to aluminosilicate silts and clays, or as coatings on silt and clay sized particulate grains. These minerals will either already have accumulated or accumulate consistent concentrations of V from seawater, before depositing in Skagerrak sediments. Any mechanism which transports fines into the basin of the Skagerrak will, in turn, transport these V-loaded Fe-(oxyhydr)oxides. For example, re-suspension of particles previously observed in the Skagerrak (Lepland and Stevens, 1996) should further enrich the basin in both V and Fe as fines are preferentially shuttled downslope by laminar bottom flows (fig. 12).

Unlike Fe, Mn certainly recycles within the Skagerrak region. Manganese diffuses out of our shelf sediments (S4, fig. 4a), presumably precipitating as fine-grained and fresh Mn-oxides in overlying seawater. Although we do not observe the efflux of Mn from our slope sediment sample, other authors report substantial Mn efflux from the slope (Danielsson, 1999; Rajendran et al., 1992). Unlike Fe-(oxyhydr)oxides, Mn-oxides therefore have a fresh supply within the Skagerrak. Indeed, our data from the Skagerrak reproduces patterns of V-Mn-oxide sequestration observed in the seawater and sediments of the Arctic basin, off the Siberian-Chukchi slope (Li et al., 2020,2021; Whitmore et al., 2019). Although we do not sample particulate Mn concentrations in the waters

867 overlying our sediments, this body of evidence supports the hypothesis that Mn-oxide precipitation
868 in Skagerrak seawater is responsible for augmenting V enrichments in the basin. The sedimentation
869 of V-enriched Mn-oxides may, in part, have a role concentrating V_{HH} in the top sediments of S9,
870 before both components are dissolved by reductive diagenesis below the ODD.

871 **5.3.3**

872 **Special role of Mn-oxides increasing $\delta^{51}V$ in the sediments of the Skagerrak basin**

873 The only $\delta^{51}V_{XS}$ values that are significantly higher than $\delta^{51}V_{Oxic}$ are located at S9 (fig. 10a) and are
874 located above the ODD, in the sediment interval with the highest V_{Total} and V_{HH} concentrations (fig.
875 3). In this depth range, Mn-oxides are enriched enough to compete with Fe-(oxyhydr)oxides as a
876 host for V in the sediment column (fig. 3, 9), and V_{HH}-Mn-oxide coupling is primarily responsible
877 for V_{XS} enrichments above that expected for Fe-(oxyhydr)oxides (fig. 11). In contrast, the $\delta^{51}V_{XS}$ at
878 S6 do not show a clear or consistent deviation from $\delta^{51}V_{Oxic}$ (fig. 10a), and V_{XS} at S6 shows no
879 unique relationship to Mn-oxides (fig. 11). From this body of evidence, we hypothesize that the
880 intense Mn-oxide enrichments present above the ODD at S9 are responsible for increasing $\delta^{51}V_{XS}$
881 values. Furthermore, V association with Mn-oxides explains why the highest $\delta^{51}V_{XS}$ values are
882 localized to top sediments at S9. We hypothesize that as these V enriched Mn-oxides are buried into
883 reducing depths, they release their relatively high $\delta^{51}V$ load into porewaters, which subsequently
884 fluxes upwards from the V porewater peak to re-enrich top sediments or efflux from the sediment
885 column.

886 The $\delta^{51}V$ composition of porewaters depends on the mechanism increasing $\delta^{51}V_{XS}$ in top sediments
887 at S9. At the time of this publication, no experimental data on V isotopic effects during diagenesis
888 have been published, and there is relatively limited data on the mechanisms that control the $\delta^{51}V$
889 composition of different (oxyhydr)oxide mineral species (Little et al., 2025). In this light, we can
890 only speculate on the Mn-oxide dependent processes that might increase $\delta^{51}V_{XS}$.

891 If V_{HH} enrichments in top sediments are partly the result of V-Mn-oxide precipitation in seawater, it
892 is plausible that the fresh precipitation of Mn-oxides in seawater may drive the observed increase in
893 $\delta^{51}V_{XS}$. For example, $\delta^{51}V_{NI*}$ ranges between -0.4 to -0.1 ‰ in hydrothermal sediments sampled
894 from the TAG hydrothermal field (Wu et al., 2022), much higher than the $\delta^{51}V_{Oxic}$ values previously
895 published from OCM and pelagic sediments (Wu et al., 2020). Hydrothermal sediments are known
896 to accumulate substantial enrichments of V through uptake by fast-precipitating Fe-
897 (oxyhydr)oxides, forming when reduced hydrothermal fluids are exposed to seawater (Feely et al.,

1998; Trefry and Metz, 1989). The rapid precipitation of V with these Fe-(oxyhydr)oxides is proposed to limit V isotope fractionation from seawater, increasing $\delta^{51}V_{NI*}$ in impacted sediments (Wu et al., 2022). Such a mechanism can conceivably be applied to the fresh V-incorporating Mn-oxides precipitating within the basin of the Skagerrak. In this case, the high $\delta^{51}V_{XS}$ of top sediments and high $\delta^{51}V_{XS}$ of S9 sediments relative to S6 sediments (fig. 10b) would be controlled by the high authigenic $\delta^{51}V_{XS}$ value of Mn-oxides sinking into the basin of the Skagerrak.

Alternatively, or as a complimentary effect, V-Mn-oxide precipitation in sediments may itself drive the observed increase in $\delta^{51}V_{XS}$. Thermodynamic calculations show that vanadyl will preferentially incorporate ^{50}V in equilibrium reactions involving either adsorption to Fe-(oxyhydr)oxide surfaces, specifically goethite, or vanadate (Wu et al., 2015). In contrast, vanadate is more prone to incorporating ^{51}V than both vanadyl and goethite (Wu et al., 2015). If vanadyl's conversion to vanadate is incomplete within the surface sediments of the Skagerrak, V-oxidation on (oxyhydr)oxide surfaces may therefore result in the preferential accumulation of ^{51}V. Indeed, Mn-oxides have been shown to be particularly effective oxidants for dissolved vanadyl (Abernathy et al., 2021). Such an effect should only operate when vanadate, and vanadate-oxide surface complexes forming in the sediment column, are stable – i.e. above the ODD. In this case, the high average $\delta^{51}V_{XS}$ of S9 sediments relative to S6 sediments (fig. 10b) necessitates a relatively low $\delta^{51}V_{XS}$ value in effluxing porewaters. Future work may target analyses of sediment porewaters above depths of diagenetic Mn-oxide precipitation to illuminate the ultimate mechanism(s) of V isotope fractionation during diagenesis.

6 Conclusion

Vanadium sequestration in deeper portions of the Skagerrak seaway is efficient, even when compared to anoxic sediment sinks (tbl. 8). Vanadium is sequestered into Skagerrak sediments by Fe-(oxyhydr)oxide particulates, concentrating in the basin with fine particulates, and may also be sequestered by Mn-oxides, possibly accumulating in the basin due to regional diagenetic Mn-cycling (fig. 12). Generally, any efflux of Fe and Mn into oxic seawater may support downslope enrichments of V in the sediment column, a process that has already been described in sediments influenced by hydrothermal plumes (Feely et al., 1998; Trefry and Metz, 1989) and along the Siberian-Chukchi margin of the Arctic Ocean (Li et al., 2021; Whitmore et al., 2019). As a rule, Mn will only be an important V sink when it is diagenetically enriched in sediments or the water column, for example due to reductive sediment diagenesis (Lovley, 1991), the formation of

ferromanganese nodules on the deep-sea floor (Calvert and Piper, 1984), or due to the shelf → basin transport of freshly precipitated Mn-oxides (Li et al., 2021). Otherwise, it will be outcompeted as a V host by the comparably ubiquitous Fe-(oxyhydr)oxide particulates present in seawater (Abernathy et al., 2022). Even in cases where Mn is extremely enriched, for example the top sediments of S9, Fe-(oxyhydr)oxide still comprise a major host for authigenic V (fig. 9). Therefore, on a global scale, Fe-(oxyhydr)oxides are probably a more important V sink than Mn-oxides. Existing mass-balances of global V-cycling characterize most of the OCM well (Little et al., 2025; Nielsen, 2021) but omit hydrography and Fe/Mn-diagenesis as a factor influencing V cycling in unrestricted water columns.

In the context of the paleo-record, V concentrations in basin sediments can be augmented by processes occurring in oxic seawater. If V enrichments in these environments are ascribed to anoxic sequestration alone, the impact of anoxia on V removal rates from seawater may be overestimated. In contrast, V isotopic signals preserved in OCM basin sediments should, following early diagenesis, roughly replicate the fractionation factor already established for oxic sediment sinks (fig. 10a). Sediment $\delta^{51}V_{NI*}$ values may therefore prove useful for establishing whether V enriched sediments were deposited beneath anoxic or oxic waters. However, we do caution that studies aiming to understand oscillations of anoxic and oxic conditions of seawater (e.g. Li et al., 2023; Wei et al., 2023) should not interpret all positive shifts in $\delta^{51}V_{NI*}$ as evidence for water column anoxia. Our data shows that such shifts may instead be related to oxide dependent diagenetic cycling, resulting in the preferential adsorption of ^{51}V in seawater or sediments.

Acknowledgements. We thank J. Blusztajin and J. Kaare-Rasmussen for assistance with isotopic analysis at Woods Hole Oceanographic Institution. T. Frickmann is thanked for assistance with sequential extractions and ICPMS analyses, and S. Risdall is thanked for assistance with ICPMS analyses, Z. Kofoed for TOC analyses, and A. Glud and H. Jensen for assistance with cruise preparations at the University of Southern Denmark. The crew of the R/V Skagerrak, P. Hall and H. Olsson from the University of Gothenburg and C. Nantke, D. Otto and A. Schell from the Leibniz-Institute for Baltic Sea Research are thanked for assistance with cruise preparations and sampling. S.G.N. acknowledges support from the National Science Foundation grant EAR-2129034. D.E.C. acknowledges support from the Villum Foundation grant 54433.

Appendix A. Supplementary Material

Supplementary figures, tables and text referenced in the article can be found in the attached supplementary materials document. All data used to generate figures, tables, and model results in this study along with quality controls are reported in nine data tables. All data, figures, tables, and supplementary files are available through figshare at https://doi.org/10.6084/m9.figshare.31267966.

Data Availability

Data are available through figshare at https://doi.org/10.6084/m9.figshare.31267966.

References

Abernathy, M.J., Schaefer, M.V., Ramirez, R., Garniwan, A., Lee, I., Zaera, F., Polizzotto, M.L., Ying, S.C., 2022. Vanadate Retention by Iron and Manganese Oxides. ACS Earth Space Chem. 6, 2041–2052. https://doi.org/10.1021/acsearthspacechem.2c00116

Abernathy, M.J., Schaefer, M.V., Vessey, C.J., Liu, H., Ying, S.C., 2021. Oxidation of V(IV) by Birnessite: Kinetics and Surface Complexation. Environ. Sci. Technol. 55, 11703–11712. https://doi.org/10.1021/acs.est.1c02464

Baes, C.F., Mesmer, R.E., 1976. The Hydrolysis of Cations, first ed. John Wiley & Sons, New York.

Bengtsson, H.K., and Stevens, R.L., 1996. Heavy-mineral provinces in southern Skagerrak and northern Kattegat. NGU Bulletin.

Bennett, W.W., Canfield, D.E., 2020. Redox-sensitive trace metals as paleoredox proxies: A review and analysis of data from modern sediments. Earth-Science Reviews 204, 103175. https://doi.org/10.1016/j.earscirev.2020.103175

Bennett, W.W., Lombi, E., Scheckel, K.G., Sekine, R., Johnston, S.G., Burton, E.D., Howard, D.L., Kappen, P., Canfield, D.E., 2023. Vanadium Speciation in Ancient Shales Revealed through Synchrotron-Based X-ray Spectroscopy. ACS Earth Space Chem. 7, 416–426. https://doi.org/10.1021/acsearthspacechem.2c00308

Boudreau, B.P., 1996. The diffusive tortuosity of fine-grained unlithified sediments. Geochimica et Cosmochimica Acta 60, 3139–3142. https://doi.org/10.1016/0016-7037(96)00158-5

Breit, G.N., Wanty, R.B., 1991. Vanadium accumulation in carbonaceous rocks: A review of geochemical controls during deposition and diagenesis. Chemical Geology 91, 83–97. https://doi.org/10.1016/0009-2541(91)90083-4

Brumsack, H.-J., 2006. The trace metal content of recent organic carbon-rich sediments: Implications for Cretaceous black shale formation. Palaeogeography, Palaeoclimatology, Palaeoecology 232, 344–361. https://doi.org/10.1016/j.palaeo.2005.05.011

Burdige, D.J., 1993. The biogeochemistry of manganese and iron reduction in marine sediments. Earth-Science Reviews 35, 249–284. https://doi.org/10.1016/0012-8252(93)90040-E

Calvert, S.E., Pedersen, T.F., 1993. Geochemistry of Recent oxic and anoxic marine sediments: Implications for the geological record. Marine Geology 113, 67–88. https://doi.org/10.1016/0025-3227(93)90150-T

Calvert, S.E., Piper, D.Z., 1984. Geochemistry of ferromanganese nodules from DOMES site a, Northern Equatorial Pacific: Multiple diagenetic metal sources in the deep sea. Geochimica et Cosmochimica Acta 48, 1913–1928. https://doi.org/10.1016/0016-7037(84)90374-0

Canfield, D.E, Jørgensen, B.B., Fossing, H., Glud, R., Gundersen, J., Ramsing, N.B., Thamdrup, B., Hansen, J.W., Nielsen, L.P., Hall, P.O.J., 1993a. Pathways of organic carbon oxidation in three continental margin sediments. Marine Geology 113, 27–40. https://doi.org/10.1016/0025-3227(93)90147-N

Canfield, Donald E., Thamdrup, B., Hansen, J.W., 1993b. The anaerobic degradation of organic matter in Danish coastal sediments: Iron reduction, manganese reduction, and sulfate reduction. Geochimica et Cosmochimica Acta 57, 3867–3883. https://doi.org/10.1016/0016-7037(93)90340-3

Chester, R., and Jickells, T., 2012. Marine Geochemistry. John Wiley and Sons. https://doi.org/10.1002/9781118349083.

Cole, D.B., Zhang, S., Planavsky, N.J., 2017. A new estimate of detrital redox-sensitive metal concentrations and variability in fluxes to marine sediments. Geochimica et Cosmochimica Acta 215, 337–353. https://doi.org/10.1016/j.gca.2017.08.004

Collier, R.W., 1984. Particulate and dissolved vanadium in the North Pacific Ocean. Nature 309, 441–444. https://doi.org/10.1038/309441a0

Crans, D.C., Amin, S.S., Keramidas, A.D., 1998. Chemistry of relevance to vanadium in the environment. In: Nriagu, J.O. (Ed.), Vanadium in the Environment. Part 1: Chemistry and Biochemistry. John Wiley & Sons, New York, pp. 73–95.

Dale, A.W., Regnier, P., Knab, N.J., Jørgensen, B.B., Van Cappellen, P., 2008. Anaerobic oxidation of methane (AOM) in marine sediments from the Skagerrak (Denmark): II. Reaction-transport modeling. Geochimica et Cosmochimica Acta 72, 2880–2894. https://doi.org/10.1016/j.gca.2007.11.039

Danielsson, Å., Cato, I., Carman, R., Rahm, L., 1999. Spatial clustering of metals in the sediments of the Skagerrak/Kattegat. Applied Geochemistry 14, 689–706. https://doi.org/10.1016/S0883-2927(99)00003-7

Diesing, M., Thorsnes, T., Bjarnadóttir, L.R., 2021. Organic carbon densities and accumulation rates in surface sediments of the North Sea and Skagerrak. Biogeosciences 18, 2139–2160. https://doi.org/10.5194/bg-18-2139-2021

Eisma, D., Kalf, J., 1987. Distribution, organic content and particle size of suspended matter in the north sea. Netherlands Journal of Sea Research 21, 265–285. https://doi.org/10.1016/0077-7579(87)90002-0

Erlenkeuser, H., Pederstad, K., 1984. Recent sediment accumulation in Skagerrak as depicted by 210pb-dating. NORSK GEOLOGISK TIDSSKRIFT.

Fan, H., Ostrander, C.M., Auro, M., Wen, H., Nielsen, S.G., 2021. Vanadium isotope evidence for expansive ocean euxinia during the appearance of early Ediacara biota. Earth and Planetary Science Letters 567, 117007. https://doi.org/10.1016/j.epsl.2021.117007

Feely, R.A., Trefry, J.H., Lebon, G.T., German, C.R., 1998. The relationship between P/Fe and V/Fe ratios in hydrothermal precipitates and dissolved phosphate in seawater. Geophys. Res. Lett. 25, 2253–2256. https://doi.org/10.1029/98GL01546

Fengler, G., Grossman, D., Kersten, M., Liebezeit, G., 1994. Trace metals in humic acids from recent Skagerrak sediments. Marine Pollution Bulletin 28, 143–147. https://doi.org/10.1016/0025-326X(94)90389-1

Froelich, P.N., Klinkhammer, G.P., Bender, M.L., Luedtke, N.A., Heath, G.R., Cullen, D., Dauphin, P., Blaynehartman, D.Hammond., 1979. Early oxidation of organic matter in pelagic sediments of the eastern equatorial Atlantic: suhoxic diagenesis 7, 1075–1090. https://doi.org/10.1016/0016-7037(79)90095-4

Gyllencreutz, R., Kissel, C., 2006. Lateglacial and Holocene sediment sources and transport patterns in the Skagerrak interpreted from high-resolution magnetic properties and grain size data. Quaternary Science Reviews 25, 1247–1263. https://doi.org/10.1016/j.quascirev.2005.11.002

Han, T., Fan, H., Wen, H., 2018. Dwindling vanadium in seawater during the early Cambrian, South China. Chemical Geology 492, 20–29. https://doi.org/10.1016/j.chemgeo.2018.05.022

Hanebuth, T.J.J., Lantzsch, H., Nizou, J., 2015. Mud depocenters on continental shelves—appearance, initiation times, and growth dynamics. Geo-Mar Lett 35, 487–503. https://doi.org/10.1007/s00367-015-0422-6

Heard, A.W., Wang, Y., Ostrander, C.M., Auro, M., Canfield, D.E., Zhang, S., Wang, H., Wang, X., Nielsen, S.G., 2023. Coupled vanadium and thallium isotope constraints on Mesoproterozoic ocean oxygenation around 1.38-1.39 Ga. Earth and Planetary Science Letters 610, 118127. https://doi.org/10.1016/j.epsl.2023.118127

Ho, P., Lee, J.-M., Heller, M.I., Lam, P.J., Shiller, A.M., 2018. The distribution of dissolved and particulate Mo and V along the U.S. GEOTRACES East Pacific Zonal Transect (GP16): The roles of oxides and biogenic particles in their distributions in the oxygen deficient zone and the hydrothermal plume. Marine Chemistry 201, 242–255. https://doi.org/10.1016/j.marchem.2017.12.003

Klaver, G.Th., van Weering, T.C.E., 1993. Rare Earth Element fractionation by selective sediment dispersal in surface sediments: the Skagerrak. Marine Geology 111, 345–359. https://doi.org/10.1016/0025-3227(93)90140-Q

Knab, N.J., Cragg, B.A., Borowski, C., Parkes, R.J., Pancost, R., Jørgensen, B.B., 2008. Anaerobic oxidation of methane (AOM) in marine sediments from the Skagerrak (Denmark): I. Geochemical and microbiological analyses. Geochimica et Cosmochimica Acta 72, 2868–2879. https://doi.org/10.1016/j.gca.2008.03.016

Kristensen, E., Røy, H., Debrabant, K., Valdemarsen, T., 2018. Carbon oxidation and bioirrigation in sediments along a Skagerrak-Kattegat-Belt Sea depth transect. Mar. Ecol. Prog. Ser. 604, 33–50. https://doi.org/10.3354/meps12734

Lepland, A., Stevens, R.L., 1996. Mineral magnetic and textural interpretations of sedimentation in the Skagerrak, eastern North Sea. Marine Geology 135, 51–64. https://doi.org/10.1016/S0025-3227(96)00060-6

Li, L., Liu, Y., Wang, X., Hu, L., Yang, G., Wang, H., Bosin, A.A., Astakhov, A.S., Shi, X., 2020. Early diagenesis and accumulation of redox-sensitive elements in East Siberian Arctic Shelves. Marine Geology 429, 106309. https://doi.org/10.1016/j.margeo.2020.106309

Li, L., Wang, X., Ren, Y., Su, H., Hu, L., Yang, G., Li, Z., Bosin, A.A., Astakhov, A.S., Chen, J., Liu, Y., Shi, X., 2021. Enrichment of Trace Metals (V, Cu, Co, Ni, and Mo) in Arctic Sediments—From Siberian Arctic Shelves to the Basin. JGR Oceans 126, e2020JC016960. https://doi.org/10.1029/2020JC016960

Li, S., Friedrich, O., Nielsen, S.G., Wu, F., Owens, J.D., 2023. Reconciling biogeochemical redox proxies: Tracking variable bottom water oxygenation during OAE-2 using vanadium isotopes. Earth and Planetary Science Letters 617, 118237. https://doi.org/10.1016/j.epsl.2023.118237

Li, S., Nielsen, S.G., Owens, J.D., 2025. Global cycling of vanadium isotopes from multiple ocean water masses and a restricted euxinic basin. Geochimica et Cosmochimica Acta 409, 82–92. https://doi.org/10.1016/j.gca.2025.08.037

Li, Y.H., and Schoonmaker, J.E., 2003. 7.01 - Chemical composition and mineralogy of marine sediments. Treatise on Geochemistry 7, 1–35. https://doi.org/10.1016/B0-08-0437516/07088-2.

Li, Y.H., Gregory, S., 1974. Diffusion of ions in sea water and in deep-sea sediments. Geochimica et Cosmochimica Acta 38, 703–714. https://doi.org/10.1016/0016-7037(74)90145-8

Little, S.H., De Souza, G.F., Xie, R.C., 2025. Metal stable isotopes in the marine realm, in: Treatise on Geochemistry. Elsevier, pp. 285–332. https://doi.org/10.1016/B978-0-323-99762-1.00019-X

Longva, O., and Thorsnes, T., 1997. Skagerrak in the past and at the present - an integrated study of geology, chemistry, hydrography and microfossil ecology. Geological Survey of Norway, Trondheim, NO.

Lovley, D.R., 1991. Dissimilatory Fe(III) and Mn(IV) reduction. Microbiol Rev 55, 259–287. https://doi.org/10.1128/mr.55.2.259-287.1991

Lu, Z., Hu, R., Han, T., Wen, H., Mo, B., Algeo, T.J., 2021. Control of V accumulation in organic-rich shales by clay-organic nanocomposites. Chemical Geology 567, 120100. https://doi.org/10.1016/j.chemgeo.2021.120100

Magnusson, K., Ekelund, R., Dave, G., Granmo, A., Forlin, L., Wennberg, L., Samuelsson, M.O, Berggren, M., Brorstrom-Lunden, E., 1996. Contamination and correlation with toxicity of sediment samples from the Skagerrak and Kattegat. Journal of Sea Research 35, 223–234.

Middelburg, J.J., Hoede, D., Van Der Sloot, H.A., Van Der Weijden, C.H., Wijkstra, J., 1988. Arsenic, antimony and vanadium in the North Atlantic Ocean. Geochimica et Cosmochimica Acta 52, 2871–2878. https://doi.org/10.1016/0016-7037(88)90154-8

Morford, J.L., Emerson, S., 1999. The geochemistry of redox sensitive trace metals in sediments. Geochimica et Cosmochimica Acta 63, 1735–1750. https://doi.org/10.1016/S0016-7037(99)00126-X

Morford, J.L., Emerson, S.R., Breckel, E.J., Kim, S.H., 2005. Diagenesis of oxyanions (V, U, Re, and Mo) in pore waters and sediments from a continental margin. Geochimica et Cosmochimica Acta 69, 5021–5032. https://doi.org/10.1016/j.gca.2005.05.015

Neaman, A., Mouélé, F., Trolard, F., Bourrié, G., 2004. Improved methods for selective dissolution of Mn oxides: applications for studying trace element associations. Applied Geochemistry 19, 973–979. https://doi.org/10.1016/j.apgeochem.2003.12.002

Nielsen, S.G., 2021. Vanadium Isotopes: A Proxy for Ocean Oxygen Variations, 1st ed. Cambridge University Press. https://doi.org/10.1017/9781108863438

Nielsen, S.G., Auro, M., Righter, K., Davis, D., Prytulak, J., Wu, F., Owens, J.D., 2019. Nucleosynthetic vanadium isotope heterogeneity of the early solar system recorded in chondritic meteorites. Earth and Planetary Science Letters 505, 131–140. https://doi.org/10.1016/j.epsl.2018.10.029

Nielsen, S.G., Prytulak, J., Halliday, A.N., 2011. Determination of Precise and Accurate 51V/50V Isotope Ratios by MC-ICP-MS, Part 1: Chemical Separation of Vanadium and Mass Spectrometric Protocols. Geostandards and Geoanalytical Research 35, 293–306. https://doi.org/10.1111/j.1751-908X.2011.00106.x

Oelkers, E.H., Gislason, S.R., Eiriksdottir, E.S., Jones, M., Pearce, C.R., Jeandel, C., 2011. The role of riverine particulate material on the global cycles of the elements. Applied Geochemistry 26, S365–S369. https://doi.org/10.1016/j.apgeochem.2011.03.062

Olesen, K.P., Nielsen, S.G., Ostrander, C.M., Udy, N., Canfield, D.E., 2025. Thallium cycling and boundary exchange in a continental margin basin. Geochimica et Cosmochimica Acta 399, 64–81. https://doi.org/10.1016/j.gca.2025.04.005

Ostrander, C.M., Owens, J.D., Nielsen, S.G., 2017. Constraining the rate of oceanic deoxygenation leading up to a Cretaceous Oceanic Anoxic Event (OAE-2: ~94 Ma). Sci. Adv. 3, e1701020. https://doi.org/10.1126/sciadv.1701020

Owens, J.D., Nielsen, S.G., Horner, T.J., Ostrander, C.M., Peterson, L.C., 2017. Thallium-isotopic compositions of euxinic sediments as a proxy for global manganese-oxide burial. Geochimica et Cosmochimica Acta 213, 291–307. https://doi.org/10.1016/j.gca.2017.06.041

Paetzel, M., Schrader, H., Bjerkli, K., 1994. Do decreased trace metal concentrations in surficial skagerrak sediments over the last 15–30 years indicate decreased pollution? Environmental Pollution 84, 213–226. https://doi.org/10.1016/0269-7491(94)90132-5

Paul, K.M., Van Helmond, N.A.G.M., Slomp, C.P., Jilbert, T., 2024. Trace metals in coastal marine sediments: Natural and anthropogenic sources, correlation matrices, and proxy potentials. Science of The Total Environment 951, 175789. https://doi.org/10.1016/j.scitotenv.2024.175789

Pederstad, K., Roaldset, E., Rønningsland, T.M., 1993. Sedimentation and environmental conditions in the inner Skagerrak-outer Oslofjord. Marine Geology 111, 245–268. https://doi.org/10.1016/0025-3227(93)90134-H

Poulton, S.W., Canfield, D.E., 2005. Development of a sequential extraction procedure for iron: implications for iron partitioning in continentally derived particulates. Chemical Geology 214, 209–221. https://doi.org/10.1016/j.chemgeo.2004.09.003

Prytulak, J., Nielsen, S.G., Halliday, A.N., 2011. Determination of Precise and Accurate 51V/50V Isotope Ratios by Multi-Collector ICP-MS, Part 2: Isotopic Composition of Six Reference Materials plus the Allende Chondrite and Verification Tests. Geostandards and Geoanalytical Research 35, 307–318. https://doi.org/10.1111/j.1751-908X.2011.00105.x

Rajendran, A., Kumar, M.D., Bakker, J.F., 1992. Control of manganese and iron in Skagerrak sediments (northeastern North Sea). Chemical Geology 98, 111–129. https://doi.org/10.1016/0009-2541(92)90094-L

Revsbech, N.P., Ward, D.M., 1983. Oxygen Microelectrode That Is Insensitive to Medium Chemical Composition: Use in an Acid Microbial Mat Dominated by *Cyanidium caldarium*. Appl Environ Microbiol 45, 755–759. https://doi.org/10.1128/aem.45.3.755-759.1983

Reyes, C., Schneider, D., Thürmer, A., Kulkarni, A., Lipka, M., Sztejrenszus, S.Y., Böttcher, M.E., Daniel, R., Friedrich, M.W., 2017. Potentially Active Iron, Sulfur, and Sulfate Reducing Bacteria in Skagerrak and Bothnian Bay Sediments. Geomicrobiology Journal 34, 840–850. https://doi.org/10.1080/01490451.2017.1281360

Rodhe, J., 1987. The large-scale circulation in the Skagerrak; interpretation of some observations. Tellus A 39A, 245–253. https://doi.org/10.1111/j.1600-0870.1987.tb00305.x

Rudnick, R.L., Gao, S., 2014. Composition of the Continental Crust, in: Treatise on Geochemistry. Elsevier, pp. 1–51. https://doi.org/10.1016/B978-0-08-095975-7.00301-6

Sæther, O.M., Faye, G., Thorsnes, T., Longva, O., n.d. Regional distribution of manganese, phosphorus, heavy metals, barium and carbon in sea-bed sediments (0-2 cm) from the northern part of the Norwegian Skagerrak. NGU Bulletin.

Scholz, F., Hensen, C., Noffke, A., Rohde, A., Liebetrau, V., Wallmann, K., 2011. Early diagenesis of redox-sensitive trace metals in the Peru upwelling area – response to ENSO-related oxygen fluctuations in the water column. Geochimica et Cosmochimica Acta 75, 7257–7276. https://doi.org/10.1016/j.gca.2011.08.007

Schulz, H.D., Zabel, M., 2006. Marine geochemistry, 2nd revised, updated and extended ed. ed. Springer, Berlin.

Schuth, S., Horn, I., Brüske, A., Wolff, P.E., Weyer, S., 2017. First vanadium isotope analyses of V-rich minerals by femtosecond laser ablation and solution-nebulization MC-ICP-MS. Ore Geology Reviews 81, 1271–1286. https://doi.org/10.1016/j.oregeorev.2016.09.028

Shaw, T.J., Gieskes, J.M., Jahnke, R.A., 1990. Early diagenesis in differing depositional environments: The response of transition metals in pore water. Geochimica et Cosmochimica Acta 54, 1233–1246. https://doi.org/10.1016/0016-7037(90)90149-F

Shieh, C., Duedall, I.W., 1988. Role of amorphous ferric oxyhydroxide in removal of anthropogenic vanadium from seawater. Marine Chemistry 25, 121–139. https://doi.org/10.1016/0304-4203(88)90060-6

Ståhl, H., Tengberg, A., Brunnegård, J., Bjørnbom, E., Forbes, T.L., Josefson, A.B., Kaberi, H.G., Hassellöv, I.M.K., Olsgard, F., Roos, P., Hall, P.O.J., 2004. Factors influencing organic carbon recycling and burial in Skagerrak sediments. J Mar Res 62, 867–907. https://doi.org/10.1357/0022240042880873

Stevens, R.L., Bengtsson, H., Lepland, A., 1996. Textural provinces and transport interpretations with fine-grained sediments in the Skagerrak. Journal of Sea Research 35, 99–110.

Taylor, S.R., McLennan, S.M., 1985. The Continental Crust: Its Composition and Evolution. Blackwell, Oxford. 312.

Takematsu, N., Sato, Y., Okabe, S., Nakayama, E., 1985. The partition of vanadium and molybdenum between manganese oxides and sea water. Geochimica et Cosmochimica Acta 49, 2395–2399. https://doi.org/10.1016/0016-7037(85)90239-X

Thamdrup, B., Dalsgaard, T., 2000. The fate of ammonium in anoxic manganese oxide-rich marine sediment. Geochimica et Cosmochimica Acta 64, 4157–4164. https://doi.org/10.1016/S0016-7037(00)00496-8

Thomson, J., Carpenter, M.S.N., Colley, S., Wilson, T.R.S., Elderfield, H., Kennedy, H., 1984. Metal accumulation rates in northwest Atlantic pelagic sediments. Geochimica et Cosmochimica Acta 48, 1935–1948. https://doi.org/10.1016/0016-7037(84)90376-4

Trefry, J.H., Metz, S., 1989. Role of hydrothermal precipitates in the geochemical cycling of vanadium. Nature 342, 531–533. https://doi.org/10.1038/342531a0

Turekian, K.K., Wedepohl, K.H., 1961. Distribution of the Elements in Some Major Units of the Earth's Crust. Geol Soc America Bull 72, 175. https://doi.org/10.1130/0016-7606(1961)72[175:DOTEIS]2.0.CO;2

van der Weijden, C.H., 2002. Pitfalls of the normalization of marine geochemical data using a common devisor. Mar. Geol. 184, 167 – 187.

van Weering, T.C.E., Berger, G.W., Kalf, J., 1987. Recent sediment accumulation in the Skagerrak, Northeastern North Sea. Netherlands Journal of Sea Research 21, 177–189. https://doi.org/10.1016/0077-7579(87)90011-1

van Weering, T.C.E., Berger, G.W., Okkels, E., 1993. Sediment transport, resuspension and accumulation rates in the northeastern Skagerrak. Marine Geology 111, 269–285. https://doi.org/10.1016/0025-3227(93)90135-I

Viers, J., Dupré, B., Gaillardet, J., 2009. Chemical composition of suspended sediments in World Rivers: New insights from a new database. Science of The Total Environment 407, 853–868. https://doi.org/10.1016/j.scitotenv.2008.09.053

Wanty, R.B., Goldhaber, M.B., 1992. Thermodynamics and kinetics of reactions involving vanadium in natural systems: Accumulation of vanadium in sedimentary rocks. Geochimica et Cosmochimica Acta 56, 1471–1483. https://doi.org/10.1016/0016-7037(92)90217-7

Wehrli, B., Stumm, W., 1989. Vanadyl in natural waters: Adsorption and hydrolysis promote oxygenation. Geochimica et Cosmochimica Acta 53, 69–77. https://doi.org/10.1016/0016-7037(89)90273-1

Wei, W., Chen, X., Ling, H.-F., Wu, F., Dong, L.-H., Pan, S., Jing, Z., Huang, F., 2023. Vanadium isotope evidence for widespread marine oxygenation from the late Ediacaran to early Cambrian. Earth and Planetary Science Letters 602, 117942. https://doi.org/10.1016/j.epsl.2022.117942

Wick, S., Baeyens, B., Marques Fernandes, M., Göttlicher, J., Fischer, M., Pfenninger, N., Plötze, M., Voegelin, A., 2020. Thallium sorption and speciation in soils: Role of micaceous clay minerals and manganese oxides. Geochimica et Cosmochimica Acta 288, 83–100. https://doi.org/10.1016/j.gca.2020.07.037

Wu, F., Owens, J.D., German, C.R., Mills, R.A., Nielsen, S.G., 2022. Vanadium isotope fractionation during hydrothermal sedimentation: Implications for the vanadium cycle in the oceans. Geochimica et Cosmochimica Acta 328, 168–184. https://doi.org/10.1016/j.gca.2022.05.002

Wu, F., Owens, J.D., Scholz, F., Huang, L., Li, S., Riedinger, N., Peterson, L.C., German, C.R., Nielsen, S.G., 2020. Sedimentary vanadium isotope signatures in low oxygen marine conditions. Geochimica et Cosmochimica Acta 284, 134–155. https://doi.org/10.1016/j.gca.2020.06.013

Wu, F., Owens, J.D., Tang, L., Dong, Y., Huang, F., 2019. Vanadium isotopic fractionation during the formation of marine ferromanganese crusts and nodules. Geochimica et Cosmochimica Acta 265, 371–385. https://doi.org/10.1016/j.gca.2019.09.007

Wu, F., Qi, Y., Yu, H., Tian, S., Hou, Z., Huang, F., 2016. Vanadium isotope measurement by MC-ICP-MS. Chemical Geology 421, 17–25. https://doi.org/10.1016/j.chemgeo.2015.11.027

Wu, F., Qin, T., Li, X., Liu, Y., Huang, J.-H., Wu, Z., Huang, F., 2015. First-principles investigation of vanadium isotope fractionation in solution and during adsorption. Earth and Planetary Science Letters 426, 216–224. https://doi.org/10.1016/j.epsl.2015.06.048

Zhu, H., Xiao, X., Guo, Z., Han, X., Liang, Y., Zhang, Y., Zhou, C., 2018. Adsorption of vanadium (V) on natural kaolinite and montmorillonite: Characteristics and mechanism. Applied Clay Science 161, 310–316. https://doi.org/10.1016/j.clay.2018.04.035

Table titles, captions, and tables

Table 1. Site locations

Tbl. 1 – Summary of sampled sites across the Skagerrak (S4 – Shelf, S6 – Slope, S9 – Basin) and a set of Norwegian rivers (R1 – Glomma, R2 - Göta Älv, R3 – Drammenselva, R4 – Otra, R5 - Nidelva). Rivers are listed in order of greatest discharge (Olesen et al., 2025).

Site	Descriptor	Latitude	Longtitude
ID	*ID*	*°N*	*°E*
S4	Shelf	57.99	9.659
S6	Slope	58.083	9.67
S9	Basin	58.413	9.678
R1	Glomma	59.294	11.137
R2	Göta Älv	57.861	11.999
R3	Drammenselva	59.749	10.164
R4	Otra	58.208	7.932
R5	Nidelva	58.434	8.725

Table 2. Sequential extraction and isotopic extraction schedule

Tbl. 2 - Summary of extraction steps, listed in the order they were applied to sediments. A single step nitric acid was applied to samples analyzed for vanadium isotopes, and this extraction is summarized below the sequential extractions. [1] – Wick et al 2020, [2] – Neamann et al 2004, [3] – Poulton and Canfield 2005, [4] – Owens et al 2017, [5] – Prytulak et al. 2011, Nielsen et al. 2011.

Extractant	Acronym	Time extracted	Temperature
ID	*ID*	*minutes*	*°C*

1 M Ammonium Acetate[1]	EC - exchangeable cations	90	Ambient
0.1 M Hydroxylamine HCl[1, 2]	HH - Hydroxylamine HCl	120	Ambient
Dithionite 50 g/L[3]	DI - dithionite	120	Ambient
2M Nitric Acid[4]	NI - nitric acid	2 x 60	130
3 HNO_3: 2 HF: 1 HCl (concentrate)	RM - residual matter	30, 20	200, 180
2M Nitric Acid[5]	NI* - nitric acid only	13 – 15 hrs	135

Table 3. Bulk physiochemistry of sediments and riverine particulates

Tbl. 3 – Physical sedimentary characteristics measured at each study site.

Site ID	Depth range *cm – cm*	Density ρ *g/mL*	*2sd*	Water content β *g/g*	*2sd*	Porosity φ	*2sd*
S4	0 – 2	1.58	*0.10*	0.40	*0.06*	0.51	*0.04*
	0 – 20	1.67	*0.16*	0.35	*0.08*	0.47	*0.06*
S6	0 – 2	1.23	*0.01*	0.68	*0.02*	0.73	*0.02*
	0 – 20	1.28	*0.10*	0.59	*0.14*	0.65	*0.11*
S9	0 – 2	1.21	*0.12*	0.73	*0.02*	0.76	*0.02*
	0 – 20	1.26	*0.12*	0.66	*0.11*	0.71	*0.09*

Table 4. Average total concentrations of TOC and Al, and Ti/Al ratios, per site

Tbl. 4 – Average TOC and Al concentrations measured from each site. [1] – Olesen et al. 2025.

Site ID	TOC[1]	*2sd*	Al	*2sd*	Ti/Al	*2sd*
	wt. %				*x10^{-2}*	
S4	0.80	*0.30*	3.75	*0.76*	6.28	0.38
S6	3.58	*0.35*	6.17	*0.32*	5.05	0.24
S9	2.95	*0.12*	7.27	*0.55*	4.53	0.69
R1			3.84		3.14	
R2			8.31		6.39	
R3			6.32		4.36	
R4			1.64		6.43	
R5			1.01		6.58	

Table 5. Percent of Al, Mn, Fe and V extracted from marine sediments by each extraction step

1222 Tbl. 5 – Percent of a given element (Al, Mn, Fe, V) liberated by a given extraction (EC, HH, DI, NI, RM; NI*) from our
1223 marine sediment samples (S4, S6, S9). Percentages are calculated relative to total elemental concentrations.

Extraction step	Al	1sd	Ti	1sd	Mn	1sd	Fe	1sd	V	1sd
EC	0	0	0	0	9	8	0	0	1	1
HH	0	0	0	0	47	32	1	1	15	7
DI	1	0	0	0	5	2	30	10	22	7
NI	31	6	8	0.3	27	20	51	7	29	7
RM	68	6	91	0.04	12	12	17	5	33	7
NI*	32	2	8	0.04	76	1	82	2	73	0.01

1224

1225 Table 6. Comparison of V_{XS} to specified extraction steps

1226 Tbl. 6 – Average percentage of V_{XS} and V_{HH+DI} contributing to V_{NI*} at each site. Minimums presented in the table
1227 represent the lower bound of V_{XS} errors presented in fig. 8. *Percentages in the top sediment of S4 (0 – 6 cm) are
1228 instead calculated relative to $V_{\sum NI}$.

Site	Depth range	V_{XS} Avg.	Min	V_{DI}/V_{XS} Avg.	1sd
ID	*cm – cm*	*% V_{NI*}*		*%*	
S4*	0 – 6	13	<0	*126*	*218*
S4	6 – 20	43	<0	*99*	*31*
S6	0 – 20	63	16	57	9
S9	0 – 20	88	59	52	5

1229

1230 Table 7. Parameters for calculating V fluxes from and into Skagerrak sediments

1231 Tbl. 7 – Variables used to calculate rates of vanadium efflux from (V_{Efflux} Rate) and rates of vanadium authigenesis in/to
1232 (V_{Auth} Rate) the sediments of the Skagerrak. Minimum V_{XS} values from S6 and S9 and average (±1sd) V_{Auth} values
1233 from S4 are used to estimate V_{Auth} Rate (tbl. 7). [1] – Li and Gregory 1974; [2] – Diesing et al. 2021.

	Efflux parameters	D_{SW} at 0 ºC	$x10^{-6}$ cm^2 s^{-1} 4.53	Sequestration parameters		
		at 25 ºC[1]	9.91			
Site	d[V]/dZ	CI	D_{Sed}	V_{XS} min.	Sed. Rate[2]	error

ID	*μg L^{-1} cm^{-1}*	*95 %*	*x10^{-6} cm^2 s^{-1}*	*μg g^{-1}*	*cm yr-1*	
S4	0.65	0.24	2.571	NA	NA	NA
S6	2.21	0.30	3.689	36	0.33	0.28
S9	1.65	0.50	3.881	105	0.33	0.24

Table 8. Net vanadium flux to the sediments of the Skagerrak

Tbl. 8 – Rates of vanadium efflux to (V_{Efflux} Rate) and rates of vanadium sequestration from (V_{Seq} Rate) the ocean. Authigenic sequestration rates into unenriched sediments underlying the OCM and enriched sediments underlying oxygen minimum zones (OMZs) are also presented. [1] – Nielsen 2021.

Site *ID*	V_{Efflux} Rate *μg cm^{-2} yr^{-1}*	error	V_{Seq} Rate *μg cm^{-2} yr^{-1}*	error
S4	+0.027	0.001	NA	NA
S6	+0.19	0.025	-7.42	7.29
S9	+0.15	0.045	-18.1	15.6
OCM[1]			-0.13	0.11 (2se)
OMZ[1]			-0.96	0.59 (2se)

Figure titles and captions

Figure 1. Site map

Fig. 1 – A) Map of the study area. Map lines delineate study areas and do not necessarily depict accepted national boundaries. Riverine samples are marked as follows: R1 – Glomma, R2 – Göta Älv, R3 – Drammenselva, R4 – Otra, R5 – Nidelva, listed in order of greatest discharge. Marine samples S4, S6, and S9 are distributed along a bathymetric profile, marked by a red line and shown in panel B.

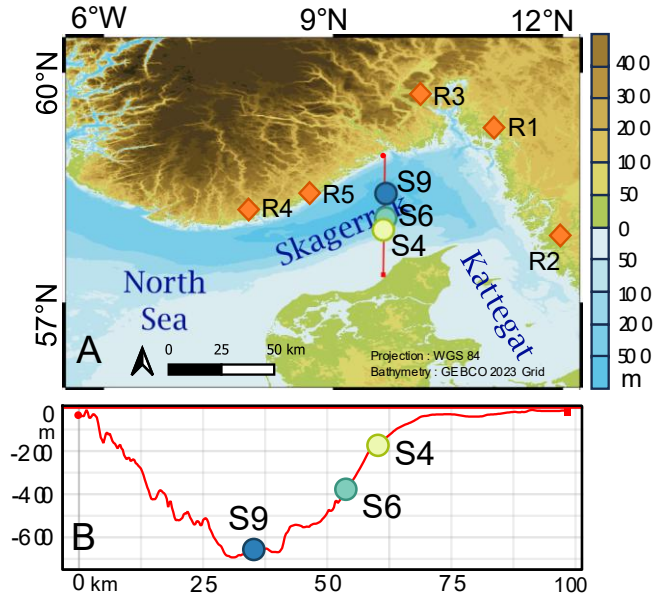

1246

1247

1248 **Figure 2. Total solid V, Fe, and Mn enrichments**

1249 Figs. 2 – Cross-plots comparing V/Al_{Total} to a) Fe/Al_{Total} and b) $\log_{10}(Mn/Al_{Total})$. Average Element/Al ratios from the
1250 upper continental crust (UCC) are provided. A linear regression and correlation factor for marine sediment data is
1251 provided in plot A (see text for description). [1] – Rudnick and Gao 2014.

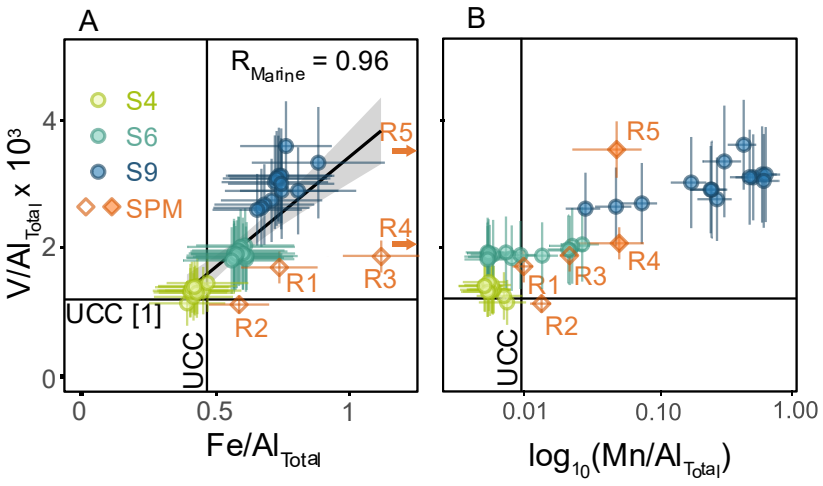

1252

1253

Figure 3. Mn, Fe, and V concentrations associated with sequential extractions

Fig. 3 – Depth distributed concentrations of Mn, Fe, and V liberated by the EC, HH, DI, NI and RM extractions. Total concentrations are the sum of all extraction steps. The oxygen depletion depth (ODD) is marked on each graph.

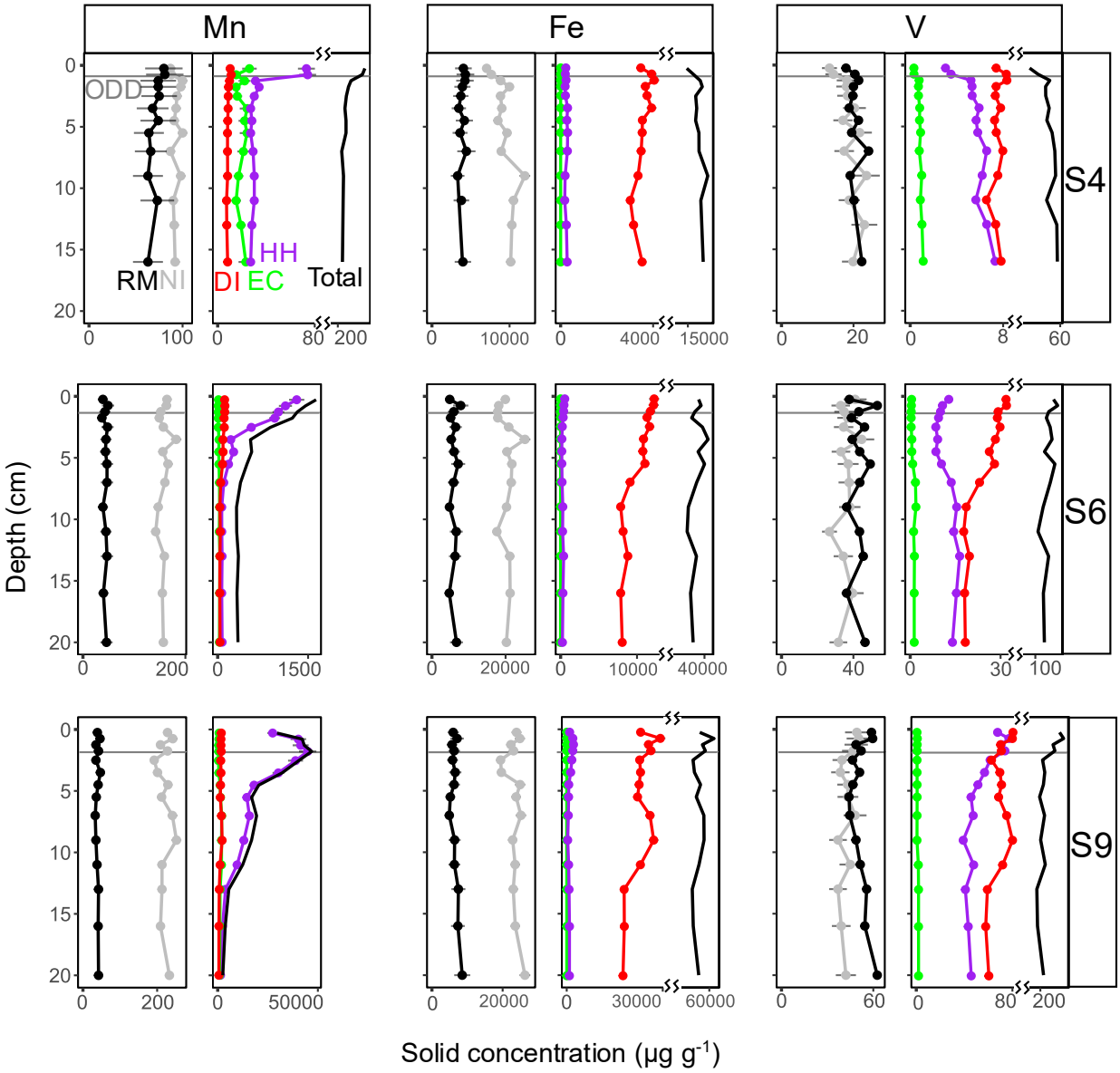

Figure 4. Mn, Fe, and V concentrations in porewater samples

Fig. 4 – Depth distributed concentrations of Mn, Fe, and V dissolved (< 0.22 µm) in porewaters separated from sediment solids by centrifugation. The oxygen depletion depths (ODD) is marked on each graph. Vanadium concentrations measured from WCS samples (red dots), bottom waters (BW, blue square) and overlying seawater (Avg. SW, black square) are also presented.

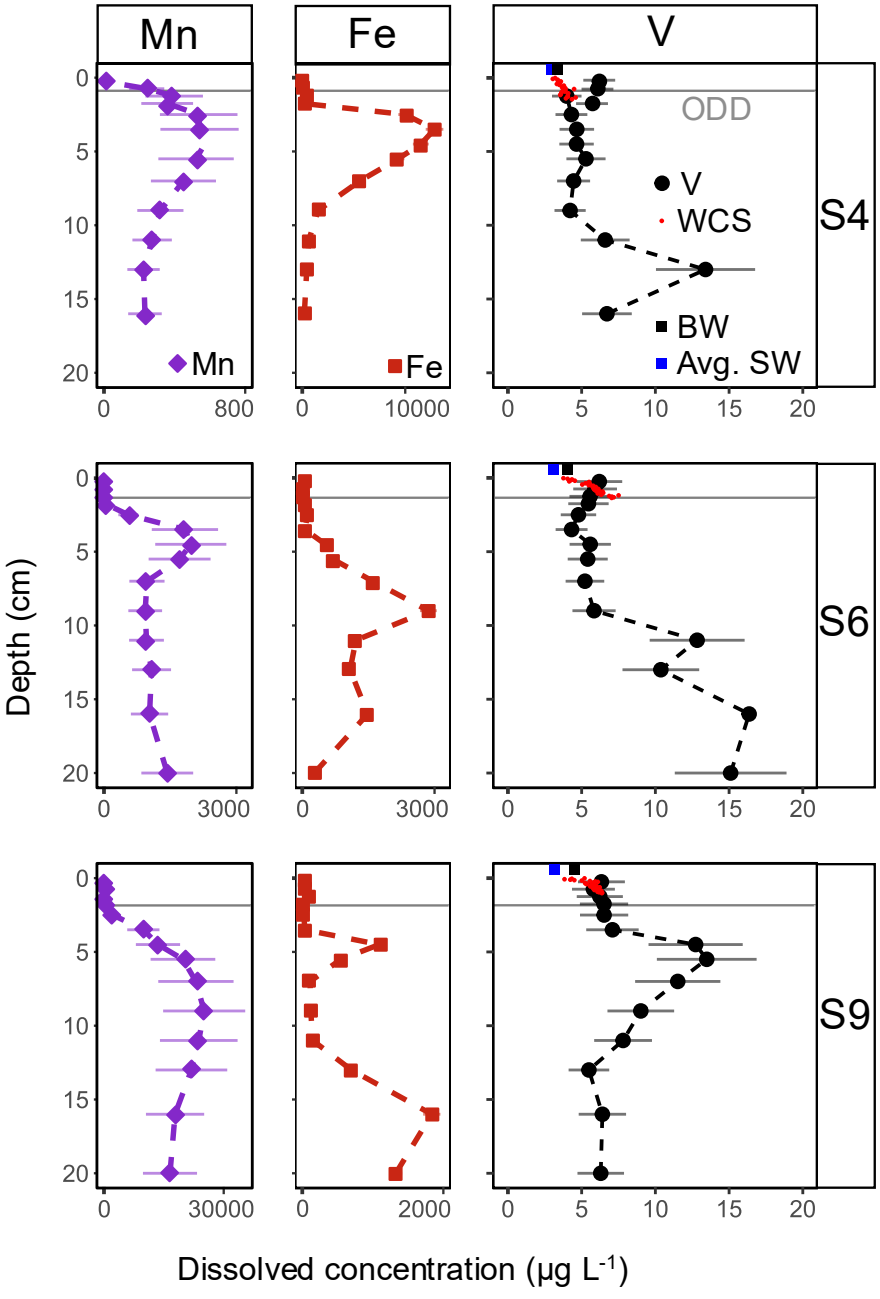

Figure 5. Correlations between dithionite liberated V and Fe

Fig. 5 – Cross-plot comparing concentrations of V and Fe liberated by the HH+DI extractions (colored dots) from all marine sediment samples and SPM. Concentrations of V and Fe liberated exclusively by DI, and a linear regression calculated using these two components from marine particulate samples, are shown in gray.

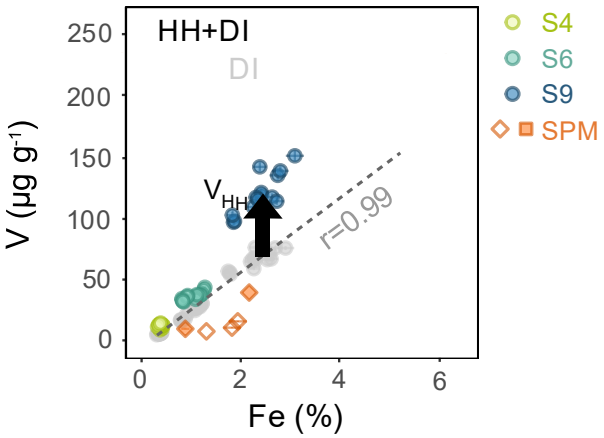

Figure 6. Vanadium liberated by single-step nitric acid extraction compared to equivalent sequential extraction steps

Fig. 6 – A) Average (±1 sd) concentrations of V liberated by specific extractions per site. Sequential extractions are stacked. Sequential extractions and the single step NI* extraction are super-imposed over V_{Total} concentrations. Two V_{NI*} averages are provided for S4: one including all measured values (dotted rectangle) and one excluding anomalous values (filled rectangle) (see text). B) Cross-plot of V vs. Al concentrations liberated by NI* (colored dots) and ∑NI (gray dots). Anomalous values at S4 are highlighted red.

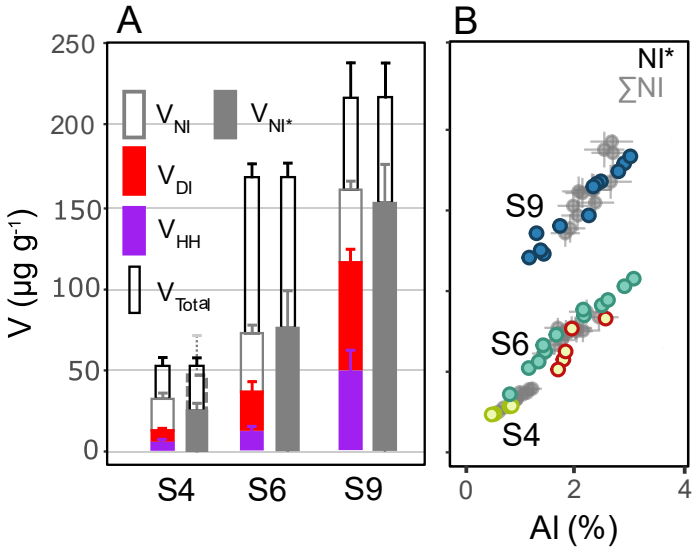

Figure 7. $\delta^{51}V_{NI*}$ of sediment samples

Fig. 7 – A) Depth distributed $\delta^{51}V_{NI*}$ values. B) Boxplots showing the mean and interquartile range of vanadium isotopes liberated by the single-step NI* extraction, pr. site. [1] – $\delta^{51}V_{NI*}$ measured from continental margin sediments underlying oxic (>50 µM O_2) waters, Wu et al. 2020; [2] – $\delta^{51}V$ measured from riverine particulates and dissolved samples (Schuth et al. 2019).

*note: offset text is not present in pdf files submitted to GCA.

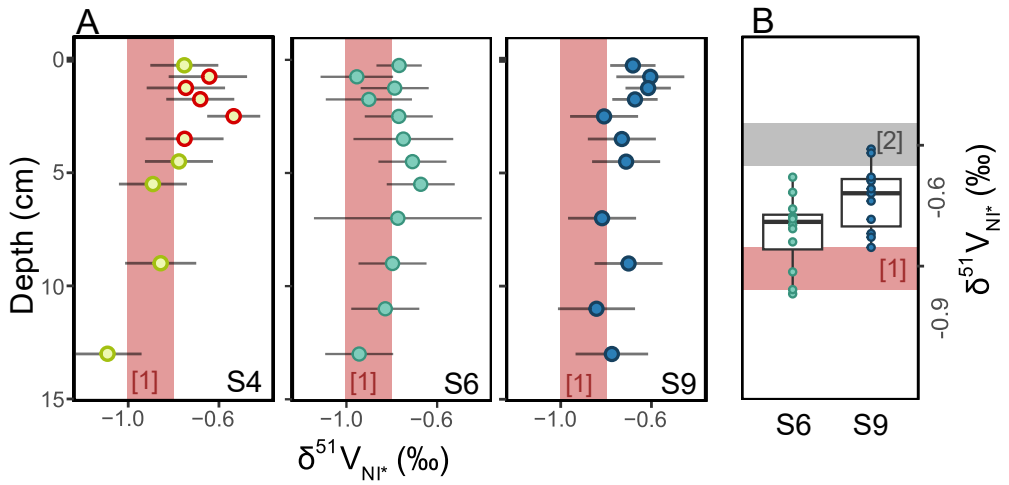

1286

1287

Figure 8. Concentration of V_{XS} compared to extraction results

Fig. 8 – Violin plots showing the concentration of V_{XS} at each site (eq. 4), calculated relative to the UCC. The uncertainty (1sd) associated with V/Al ratios from the UCC is labelled on the diagram as a black line. The V_{XS} of SPM from the meandering rivers sampled by Olesen et al. (2025) are labelled as orange bars. The average (±1 sd) concentration of V liberated by HH+DI and NI*, respectively, are labelled for each site.

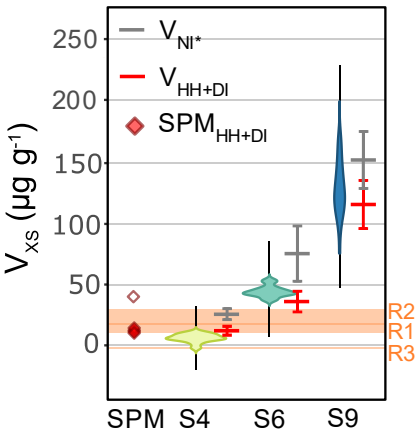

Figure 9. Speciation of excess vanadium with depth

Fig. 9 – Depth plot comparing the concentration of V_{DI}, V_{HH}, liberated by sequential extraction, to V_{XS} across sediment depths at the V enriched sites S6 and S9. Concentrations of V_{HH} and V_{DI} are stacked.

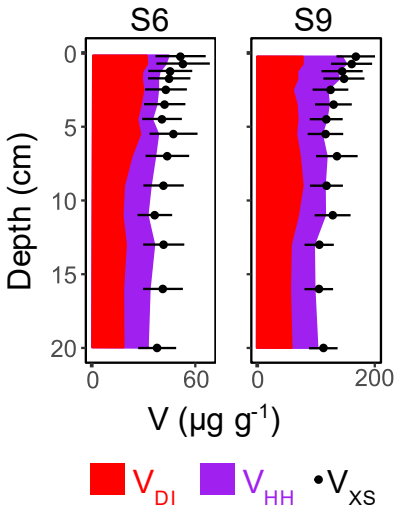

Figure 10. Estimation of $\delta^{51}V_{XS}$

Fig. 10 – A) Depth plots comparing $\delta^{51}V_{XS}$ (colored dots) to $\delta^{51}V_{NI*}$ (grey dots) for S6 and S9. B) Boxplots showing the mean and interquartile range of $\delta^{51}V_{XS}$, for S6 and S9 (eq. 6); the mean value calculated from $\delta^{51}V_{NI*}$ (fig. 7b) is shown as a black bar. [1] – $\delta^{51}V_{NI*}$ measured from continental margin sediments underlying oxic (>50 µM O_2) waters, Wu et al. 2020; [2] – $\delta^{51}V$ measured from riverine particulates and dissolved samples (Schuth et al. 2019).

*note: offset text is not present in pdf files submitted to GCA.

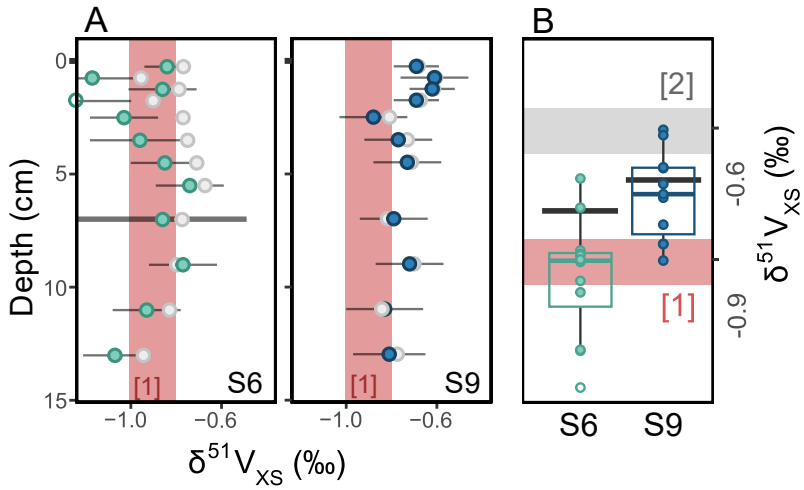

Figure 11. Distinct total V/Fe ratios from riverine SPM, S4+S6, and S9

Fig. 11 – Cross-plots comparing concentrations of V and Fe from all marine sediment samples and SPM liberated by all extraction steps. The average V/Fe ratios of samples from S4+S6, and of SPM samples, are plotted separately.

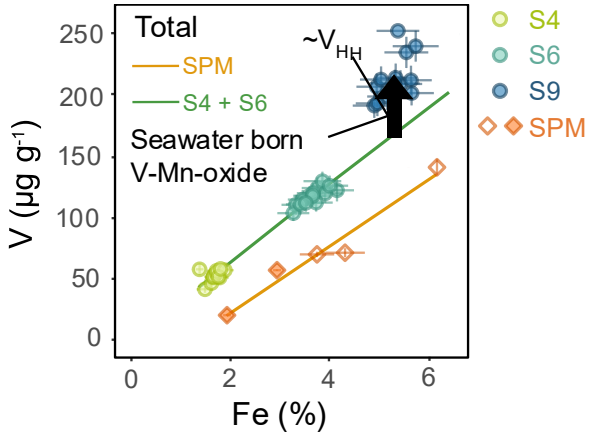

Figure 12. V sensitivity to Fe/Mn-inflows into the basin of the Skagerrak

Fig. 12 – Cartoon summarizing the processes influencing vanadium's enrichment moving into the basin of the Skagerrak seaway. Birnessite and ferrihydrite are used as model Mn-oxides and Fe-(oxyhydr)oxides, respectively.

*note: offset text is not present in pdf files submitted to GCA.

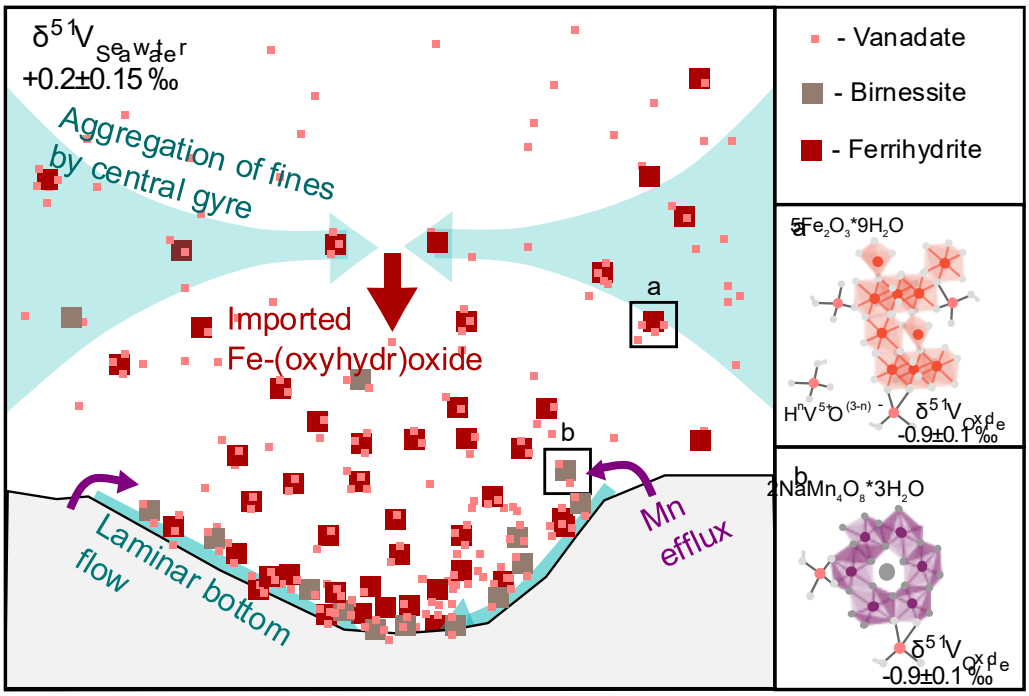

Supplementary text, tables, and figures for the manuscript entitled

Exploring the sensitivity of the vanadium redox proxy to Fe/Mn-(oxyhydr)oxide cycling in a basinal oxic margin setting

Nicol. D. Udy[1*], Sune G. Nielsen[2,3], Maureen Auro[2], Kasper P. Olesen[1], Donald E. Canfield[1]

[1] Department of Biology, Nordcee, University of Southern Denmark, Odense, Denmark

[2] Department of Geology and Geophysics, Woods Hole Oceanographic Institution, Woods Hole, MA, USA

[3]Centre de Recherches Pétrographiques et Géochimiques, CNRS, Université de Lorraine, Nancy, France

* nicoldudy_phd_correspondence@proton.me (corresponding author)

1331 Supplement 1. Whole core squeezing notes and methodology

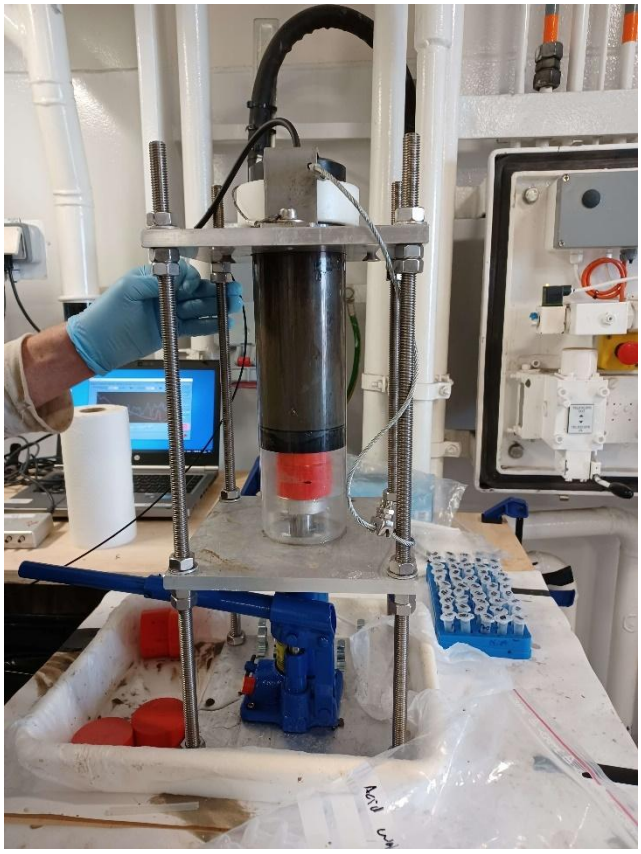

Fig. S1 – Picture of the whole core squeezing apparatus. Core is secured between two metal plates, after being fitted against a PVC plastic plate using a rubber gasket and plastic ring (white) at the top. A small plastic valve is attached to isoversinic tubing at the top of the device (obscured by metal tab), connected to the SWI through a small hole drilled in the PVC plastic plate. After installation, the core is compressed using the hydraulic jack (blue, at bottom of apparatus), forcing water out of the top sediments. The device is designed to extract the top 1 – 2 cm of water in sub 1/10th of a centimeter intervals.

1343

1344 Whole core squeezing platforms are applied to soft, unconsolidated sediments for the extraction of
1345 finely resolved porewater profiles. A picture and description of our platform is available in figure
1346 S2. For examples of similar whole core squeezing platforms, please refer to Schulz and Zabel 2006
1347 (section 3.2.2). The depth of each sample extruded using the apparatus depicted in figure S2 must
1348 be estimated. Heights of the core pre- and post-compression were recorded for calculation of
1349 sample depths assuming laminar flow during porewater extraction. Sample depths (Depth, cm) were
1350 calculated:

1351 $$Depth = (n * V - 1)/(\pi * r^2 * \beta) \quad \text{eq. S1}$$

1352 by multiplying the sample number (n, n = 0 being the sediment surface) by the volume sampled (V,
1353 1.8 cm^3) and dividing the resulting value by the inner area of the core liner (π * r^2, r = 3.85 cm) and
1354 the water content of the sample (β, tbl. 3).

1355

Supplement 2. Rationale and methodology for extracting and isolating V for isotope analysis

Partial leaching of all samples was performed to isolate authigenically precipitated V from terrigenous V delivered into marine sediments by continental detritus. The selected leaching procedure is designed to leave aluminosilicate phases undissolved, while targeting organic matter, oxide minerals, and sulfide minerals, each of which may host V following authigenesis in seawater or sediments (Haase et al. 2024, Ohnemus et al. 2017, Calvert et al. 2015, Trefry and Metz 1989). Authigenic V forming in oxic seawater is expected to precipitate through adsorption on (oxyhydr)oxide minerals (Little et al. 2025). The vanadium isotopic composition of marine sediments depositing beneath oxic seawater ($\delta^{51}V_{Oxic}$ = -0.9 ± 0.1 ‰; Wu et al. 2020) is lower than the isotopic composition of V carried by riverine particulate matter (Schuth et al. 2019). The high detrital V contents present in most marine samples may therefore obscure authigenic signals, resulting in an unreasonably high isotopic value in bulk digested sediment samples (e.g. Wu et al. 2020). While partial leaching may not dissolve all authigenic phases or may be able to dissolve terrigenous phyllo-silicate clay minerals (Wu et al. 2020), it has been shown to adequately separate authigenic V from detrital V in both modern (Wu et al. 2020) and ancient (Fan et al. 2021, Nielsen et al. 2019, Ostrander et al. 2017). However, the efficacy of the partial leaching method may depend on the relative concentration of authigenic V present in a sample (Wu et al. 2020). For this reason, extraction results should be interpreted carefully to ensure that measured isotopic values are controlled by authigenic processes, either in seawater or due to diagenesis in sediments.

Between 70 and 100 mg of dried sediment and USGS shale standard SCo-1 were subsampled from freeze-dried stocks, and each subsample was ground in a pure quartz mortar and pestle into a fine powder. Powdered samples were leached in 3 mL 2M twice distilled HNO_3 overnight (13 – 15 hours). Samples near the sediment water interface were prioritized for analysis when sufficient sample mass was available. Powdered sediments samples and were digested in TM-clean Teflon vessels using 2 M nitric acid, at 130 ºC for 13 – 15 hours. Remaining solids were separated from the leaching solution by pipetting out the supernatant following centrifugation, and this step was repeated three times to ensure complete separation of solid-residual and digested V. After separation from the nitric acid, the leachate was extracted in inverse aqua-regia and hydrogen peroxide at 130 ºC to digest any remaining organic matter. The nitric acid supernatant and aqua-regia supernatant were mixed and dried to a pellet on a hot plate. Sample pellets were then dissolved in 0.1 M M HNO_3, and aliquots were taken for measurement of digested V concentrations (see method).´From

the 10 mL stock, 100 µL of sample was diluted with 1800 µL 2% HNO_3 and 100 µL of 2% HNO_3 seeded with 20 ppb of In. These aliquots were analyzed on a Thermo-Finnigan iCAP quadrapole ICP-MS, and resulting elemental abundances are referred to using the extraction code NI*.

Vanadium was separated from the remaining sample matrix using cationic exchange resin AG-50W-X12 (once) and anionic exchange resin AG1X8 (twice) following previously outlined methods (Nielsen et al. 2019). After each V separation, while V was still loaded onto the resin, the V-free eluted solution was collected. This V-free elution was analyzed to ensure no V was lost during separation and prior to V elution. Less than 2 % of V from each sample was lost compared to the initial leach. After collection on the resin and the removal of the V-free elution, vanadium was rinsed off of the resin using 10 mL 6M TM-pure hydrochloric acid in 12 mL Teflon vials, before being prepared for the next resin isolation step.

Supplement 3. Data quality issues and equivocal interpretations regarding the S4 isotope data set

The single step nitric acid extraction employed in our study is commonly used to isolate authigenic V from V delivered by detrital phases (e.g. Fan et al. 2021, Wu et al. 2020, Nielsen et al. 2019, Ostrander et al. 2017). The confident application of this extraction requires that V be sufficiently enriched above the crustal background such that partial dilution of detrital phases does not impact the measurement of $\delta^{51}V$ (Wu et al. 2020), and that authigenic V is primarily associated with processes of seawater sequestration rather than post-depositional diagenesis (Bennett et al. 2023).

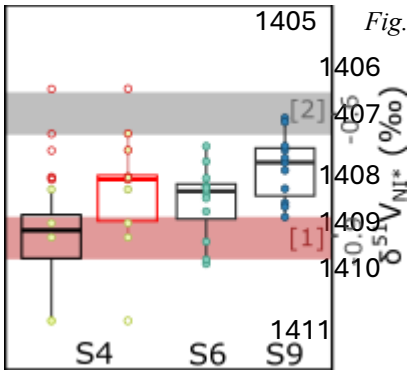

Fig. S3-1 – Boxplots showing the mean and interquartile range of vanadium isotopes liberated by the single-step NI extraction, pr. site. Depending on the treatment of anomalous data, S4 produces significantly different mean $\delta^{51}V_{NI*}$ values. [1] – $\delta^{51}V_{NI*}$ measured from continental margin sediments underlying oxic (>50 µM O_2) waters, Wu et al. 2020; [2] – $\delta^{51}V_{NI*}$ of sediments depositing beneath anoxic (< 10 µM O_2) seawater, Wu et al. 2020*

At S4, 5 five samples relatively shallow in the sediment column (fig. 6a, see text) produce higher $\delta^{51}V_{NI*}$ values than other samples. Indeed, one of these samples, located at 4.5 cm, is significantly deviated from the $\delta^{51}V_{Oxic}$ value measured previously at oxic sites (Wu et al. 2020). These samples also show concentration anomalies, such that the concentration of V evidently liberated by the single step nitric acid extraction (V_{NI*}) is higher than the sum total of V measured from our sequential extraction procedure (fig. 5, tbl. S4). The mean isotopic value calculated for S4 varies significantly depending on whether or not these anomalous samples are included (fig. S4-1). This supplement explains the likely cause of this concentration anomaly and addresses whether or not the isotopic data measured from S4 can be confidently treated as authigenic.

The five samples which are impacted by the concentration anomaly do not only show high V_{NI*} values. Table S4 shows that Mn and Fe liberated by NI* are also higher than their sum concentration from our sequential extraction procedure and NI* liberated Al concentrations in the suspect samples are about 2-fold higher than in unimpacted samples. This trend extends to many other transitions metals, including Cr, Co, U, and Mo. Furthermore, unimpacted samples show NI* liberated Al, V, Mn, and Fe comparable to those liberated by ∑NI, as was expected (see text). It is

difficult to explain how all elements in the suspect samples could be contaminated, to produce such anomalously high enrichments for many elements. Instead of contamination, a universal, systematic increase in general elemental abundances implies these samples were more concentrated than recorded when initially analyzed for their elemental abundance. After sediments were leached by the NI* step, a 100 µL aliquot of the 2 mL HNO_3 diluted sample was analyzed for total elemental concentration (supplement 2). This sample should have been diluted 20x, and this dilution factor was used to estimate the elemental concentration present in each sample. If there was a pipetting error, either when taking up the sample aliquot or when diluting the sample for analysis, then final elemental concentrations calculated for the NI* extraction step may be higher than is realistic. The relatively high $\delta^{51}V$ values measured from the anomalous S4 samples therefore cannot confidently be rejected as contaminated or incorrectly measured.

Sample	Al			Fe			V			Mn		
ID	NI*	∑NI	Sum	NI*	∑NI	Sum	NI*	∑NI	Sum	NI*	∑NI	Sum
	wt. %			*wt. %*			*µg g^{-1}*			*µg g^{-1}*		
S4-1	0.8	0.7	3.7	1.2	1.1	1.5	29	24	42	239	196	276
S4-2	2.6	0.7	3.8	3.1	1.2	1.6	83	26	47	351	188	269
S4-3	1.8	0.9	4.1	2.1	1.3	1.7	58	32	54	197	163	236
S4-4	1.7	1.0	3.9	1.9	1.4	1.8	51	31	51	183	156	230
S4-5	2	1.0	3.9	2.8	1.3	1.6	77	32	51	229	149	224
S4-6	1.9	1.1	3.8	2.2	1.3	1.7	63	35	53	212	152	220
S4-7	1.3	0.8	4	1.7	1.2	1.7	44	31	31	174	149	223
S4-8	0.9	1.1	4.1	1.2	1.3	1.7	29	36	36	148	159	223
S4-10	0.5	1.3	4.0	0.9	1.6	1.9	24	38	57	133	153	211
S4-12	0.5	1.2	NA	0.9	1.4	NA	24	38	58	132	142	216

Tbl. S3 – Aluminum, Fe, V and Mn concentrations liberated by the NI single step extraction, liberated by the EC+HH+DI+NI sequential extraction steps (∑NI), and liberated by all extraction steps (sum) from marine sampling site S4. Highlighted samples have higher Fe, V, and Mn concentrations liberated by NI* than the sum concentration of all extraction steps.*

However, as stated in the text, all but one of these samples is still within error of $\delta^{51}V_{Oxic}$ (fig. 6a). Furthermore, as stated in supplement 2, the efficacy of the partial leaching method used to extract V for isotopic analysis is dependent on the relative concentration of authigenic V present in a sample (Wu et al. 2020). When V contents are near the continental background, the partial dilution of detrital material by nitric acid may result in an unrealistically high authigenic $\delta^{51}V_{NI*}$. We suspect that our nitric acid extractions (NI and NI*) may have dissolved clay minerals, particularly illite

(Olesen et al. 2025), explaining the unusually high portion of Al liberated by nitric acid by our sequential extractions (see tbl. 5 in $_{text}$).

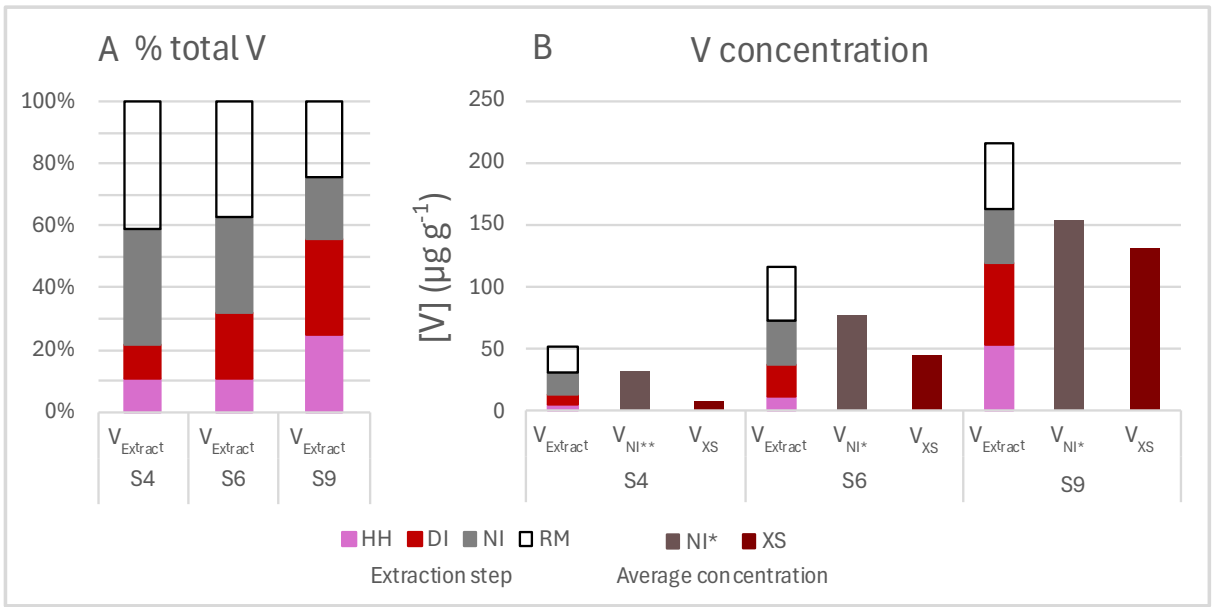

Fig. S3-2 – A) site averaged portion of total V liberated by each extractions step and B) bar plots comparing the site averaged concentration of V liberated by each extraction step to the concentration of V liberated by NI, and the concentration of V in excess (XS) of the continental background (see text). The V_{NI**} average calculated at S4 only uses samples which are not impacted by the concentration anomaly described above.*

Indeed, the total portion of V associated with Al-free mineral phases, e.g. those dissolved by the HH and DI extraction steps (tbl. 5) is approximately 20 % at S4, while exceeding 30 % and 50 % at S6 and S9, respectively (fig. S4-2a). When considering samples not impacted by the concentration anomaly described above, V_{NI*} consistently produces a V concentration comparable to $V_{\sum NI}$ (i.e. the sum of the HH + DI + NI extractions). At S6 and S9, 57% and 85% of V_{NI*} is accounted for by V_{XS}, respectively. The value V_{XS} represents the concentration of V which is likely not delivered by continental detritus (see text). In contrast, V_{XS} represents only 20% of V_{NI*} at S4, and V_{XS} does not account for the concentration of V liberated from Al-free phases (HH + DI). In other words, it is unlikely that there is enough authigenic V present at S4 to prevent the dilution of $\delta^{51}V_{NI*}$ by a partial leach of detrital matter during the NI* extraction. In contrast, $\delta^{51}V_{NI*}$ values at S6 and especially at S9 can be more confidently attributed to non-detrital inputs. The potential influence of post-depositional processes to $\delta^{51}V_{NI*}$ values measured from S6 and S9 is addressed in text.

Supplement 4. Comments on the solid phases plausibly relevant to vanadium dissolved by our extractions

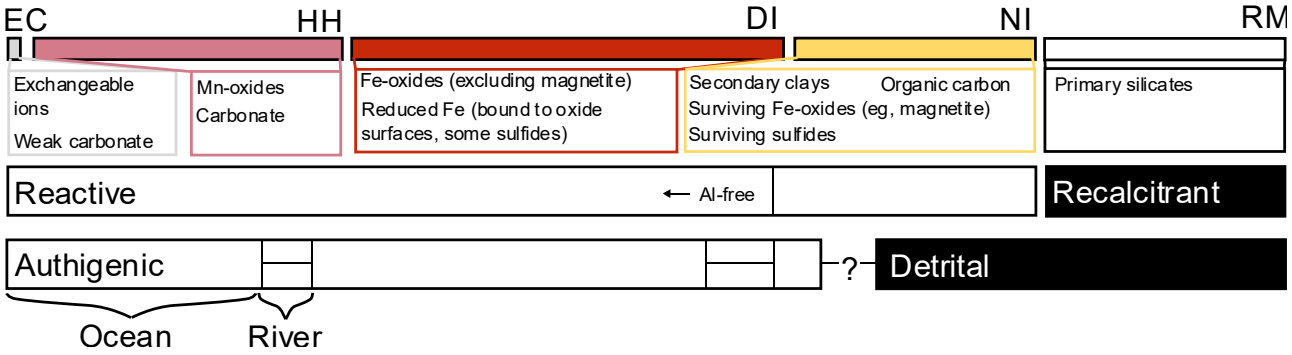

Fig. S4 – Diagram labelling likely solid phases liberated by each of our extraction steps. The chemical codification of these extractions (eg. reactive, recalcitrant) and the presumable source of the elements liberated by each extraction step are also provided (see text).

Our sequential extraction methodology was designed to separately dissolved Mn-oxides (HH step) and Fe-(oxyyhydr)oxides (DI step), and to entirely omit detrital aluminosilicate minerals from reactive extractions (EC + HH + DI + NI). However, each extraction step may dissolve other phases known to host V. The most relevant phases to our methodology and interpretations are addressed in detail below.

Acidity of the EC and HH extraction steps results in the dissolution of Ca-bearing minerals, presumably carbonates. Carbonates incorporate V^{3+}, following reduction of vanadium in sediment porewaters (Breit and Wanty 1991). Therefore, a portion of V interpreted to associate with Mn-oxides may in fact be bound by carbonate phases following diagenesis. At S9, where Mn is almost completely associated with Mn-oxides for the sampled depth range (Canfield et al. 1993a,b) and Mn-oxides are hyper-enriched above 15 cm sediment depth (fig. S5), there is little reason to expect that high portions of the V liberated by HH are associated with carbonates. At S6, Mn-oxides are obviously enriched in the top 5 cm of the sediment column (Canfield et al. 1993a,b; fig. S5), but below this depth V may well be hosted by carbonate phases rather than Mn-bearing oxides. Finally, at S4, Mn is only slightly enriched in the top cm (Canfield et al. 1993a,b; fig. S5) and is in fact depleted relative to the UCC through most of the sediment column (tbl. 4). In these sediments, V may well be associated with carbonates rather than Mn-oxides through the entire sediment column.

Dithionite may dissolve Fe-bearing sulfides, except for pyrite (Poulton and Canfield 2005). Sulfides are capable of hosting V (Haase et al. 2024) following the dissolution of Fe-(oxyhydr)oxides and reduction of sorbed V, resulting in mineral complexes incorporating Fe^{2+} and $V^{3/4+}$, respectively.

Iron bearing sulfide minerals were not observed within the 10 cm depth range sampled by Canfield et al. (1993a,b), but they may still accumulate below 10 cm in our own samples. Because V sorbs to both Fe-(oxyhydr)oxides and Fe-sulfides, the transformation of oxides to sulfides with depth may obscure both the reduction of V and the reduction of Fe in our own depth profiles – in other words, dithionite liberated V and Fe does not help us distinguish, across depth, between oxide bound V and sulfide bound V.

Supplementary references

Bennett, W. W., Lombi, E., Scheckel, K. G., Sekine, R., Johnston, S. G., Burton, E. D., Howard, D. L., Kappen, P., & Canfield, D. E. (2023). Vanadium Speciation in Ancient Shales Revealed through Synchrotron-Based X-ray Spectroscopy. *ACS Earth and Space Chemistry*, *7*(2), 416–426. https://doi.org/10.1021/acsearthspacechem.2c00308

Breit, G. N., & Wanty, R. B. (1991). Vanadium accumulation in carbonaceous rocks: A review of geochemical controls during deposition and diagenesis. *Chemical Geology*, *91*(2), 83–97. https://doi.org/10.1016/0009-2541(91)90083-4

Calvert, S. E., Piper, D. Z., Thunell, R. C., & Astor, Y. (2015). Elemental settling and burial fluxes in the Cariaco Basin. *Marine Chemistry*, *177*, 607–629. https://doi.org/10.1016/j.marchem.2015.10.001

Canfield, D. E., Jørgensen, B. B., Fossing, H., Glud, R., Gundersen, J., Ramsing, N. B., Thamdrup, B., Hansen, J. W., Nielsen, L. P., & Hall, P. O. J. (1993a). Pathways of organic carbon oxidation in three continental margin sediments. *Marine Geology*, *113*(1–2), 27–40. https://doi.org/10.1016/0025-3227(93)90147-N

Canfield, D. E., Thamdrup, B., & Hansen, J. W. (1993b). The anaerobic degradation of organic matter in Danish coastal sediments: Iron reduction, manganese reduction, and sulfate reduction. *Geochimica et Cosmochimica Acta*, *57*(16), 3867–3883. https://doi.org/10.1016/0016-7037(93)90340-3

Fan, H., Ostrander, C. M., Auro, M., Wen, H., & Nielsen, S. G. (2021). Vanadium isotope evidence for expansive ocean euxinia during the appearance of early Ediacara biota. *Earth and Planetary Science Letters*, *567*, 117007. https://doi.org/10.1016/j.epsl.2021.117007

Haase, F. J., Vessey, C. J., Sekine, R., Doriean, N. J. C., Welsh, D. T., Otte, J. A., Hamilton, J., Canfield, D. E., Wang, Y., Lombi, E., & Bennett, W. W. (2024). Reductive sorption of vanadium by iron monosulfide in seawater. *Chemical Geology*, *649*, 121983. https://doi.org/10.1016/j.chemgeo.2024.121983

Little, S. H., De Souza, G. F., & Xie, R. C. (2025). Metal stable isotopes in the marine realm. In *Treatise on Geochemistry* (pp. 285–332). Elsevier. https://doi.org/10.1016/B978-0-323-99762-1.00019-X

Nielsen, S. G., Auro, M., Righter, K., Davis, D., Prytulak, J., Wu, F., & Owens, J. D. (2019). Nucleosynthetic vanadium isotope heterogeneity of the early solar system recorded in chondritic meteorites. *Earth and Planetary Science Letters*, *505*, 131–140. https://doi.org/10.1016/j.epsl.2018.10.029

Ohnemus, D. C., Rauschenberg, S., Cutter, G. A., Fitzsimmons, J. N., Sherrell, R. M., & Twining, B. S. (2017). Elevated trace metal content of prokaryotic communities associated with marine oxygen deficient zones: Elevated trace metals in ODZ prokaryotes. *Limnology and Oceanography*, *62*(1), 3–25. https://doi.org/10.1002/lno.10363

Olesen, K. P., Nielsen, S. G., Ostrander, C. M., Udy, N., & Canfield, D. E. (2025). Thallium cycling and boundary exchange in a continental margin basin. *Geochimica et Cosmochimica Acta*, *399*, 64–81. https://doi.org/10.1016/j.gca.2025.04.005

Ostrander, C. M., Owens, J. D., & Nielsen, S. G. (2017). Constraining the rate of oceanic deoxygenation leading up to a Cretaceous Oceanic Anoxic Event (OAE-2: ~94 Ma). *Science Advances*, *3*(8), e1701020. https://doi.org/10.1126/sciadv.1701020

Poulton, S. W., & Canfield, D. E. (2005). Development of a sequential extraction procedure for iron: Implications for iron partitioning in continentally derived particulates. *Chemical Geology*, *214*(3–4), 209–221. https://doi.org/10.1016/j.chemgeo.2004.09.003

Rudnick, R. L., & Gao, S. (2014). Composition of the Continental Crust. In *Treatise on Geochemistry* (pp. 1–51). Elsevier. https://doi.org/10.1016/B978-0-08-095975-7.00301-6

Schuth, S., Brüske, A., Hohl, S. V., Jiang, S.-Y., Meinhardt, A.-K., Gregory, D. D., Viehmann, S., & Weyer, S. (2019). Vanadium and its isotope composition of river water and seawater: Analytical improvement and implications for vanadium isotope fractionation. *Chemical Geology*, *528*, 119261. https://doi.org/10.1016/j.chemgeo.2019.07.036

Trefry, J. H., & Metz, S. (1989). Role of hydrothermal precipitates in the geochemical cycling of vanadium. *Nature*, *342*(6249), 531–533. https://doi.org/10.1038/342531a0

Wu, F., Owens, J. D., Scholz, F., Huang, L., Li, S., Riedinger, N., Peterson, L. C., German, C. R., & Nielsen, S. G. (2020). Sedimentary vanadium isotope signatures in low oxygen marine conditions. *Geochimica et Cosmochimica Acta*, *284*, 134–155. https://doi.org/10.1016/j.gca.2020.06.013